

Estimation of 1 km downwelling shortwave radiation over the Tibetan Plateau under all-sky conditions

Peizhen Li¹, Lei Zhong^{1,2,3,4}, Yaoming Ma^{5,6,7,8,9,10}, Yunfei Fu¹, Meilin Cheng¹, Xian Wang¹, Yuting Qi¹, Zixin Wang¹

5 ¹School of Earth and Space Sciences, University of Science and Technology of China, Hefei 230026, China

²CAS Center for Excellence in Comparative Planetology, Hefei 230026, China

³Jiangsu Collaborative Innovation Center for Climate Change, Nanjing 210023, China

10 ⁴Frontiers Science Center for Planetary Exploration and Emerging Technologies, University of Science and Technology of China, Hefei 230026, China

⁵Land-Atmosphere Interaction and its Climatic Effects Group, State Key Laboratory of Tibetan Plateau Earth System, Resources and Environment (TPESRE), Institute of Tibetan Plateau Research, Chinese Academy of Sciences, Beijing 100101, China

15 ⁶College of Earth and Planetary Sciences, University of Chinese Academy of Sciences, Beijing 100049, China

⁷College of Atmospheric Science, Lanzhou University, Lanzhou 730000, China

⁸National Observation and Research Station for Qomolangma Special Atmospheric Processes and Environmental Changes, Dingri 858200, China

⁹Kathmandu Center of Research and Education, Chinese Academy of Sciences, Beijing 100101, China

20 ¹⁰China-Pakistan Joint Research Center on Earth Sciences, Chinese Academy of Sciences, Islamabad 45320, Pakistan

Correspondence to: Lei Zhong (zhonglei@ustc.edu.cn)

Abstract. Downwelling shortwave radiation (DSR) is the basic driving force for the energy and water cycles of the Earth's climate system. As called the Third Pole of the Earth, the Tibetan Plateau (TP) absorbs a large amount of shortwave radiation and exert important impacts on global weather and climate change. However, due to coarse spatial resolution and insufficient consideration of factors influencing radiative transfer processes, DSR parameterization schemes are still need to be improved when applied to the TP. Based on satellite datasets and meteorological forcing data, all-sky DSR over the TP at a spatial resolution of 1 km was derived using an improved parameterization scheme. The influence of topography and different radiative attenuations were comprehensively taken into account. Specifically, the introduction of cloud multiscattering and topography factors further improves the DSR estimation accuracy. The validation results indicated that the developed parameterization scheme showed reasonable accuracy. By comparing with current widely used DSR products based on the same in situ observations, the derived DSR performed much better on different spatial and temporal scales. On

25
30

35 instantaneous, ten-day, and monthly timescales, the root-mean-square errors (RMSEs) of the derived
DSR are 132.8~158.2 W m⁻², 70.8~76.5 W m⁻², and 61.3~67.5 W m⁻², respectively, which are much
smaller than those of current DSR products. The derived DSR not only captured the temporal variation
characteristics that are more consistent with the in situ measurements, but also provided reasonable
spatial patterns. Meanwhile, the proposed parameterization scheme demonstrated its superiority in
40 characterizing more details and high dynamics of the spatial pattern of DSR due to its terrain correction
and high resolution. Moreover, this parameterization scheme does not need any local correction in
advance and it has the potential to be extended to other regions in the world.

1 Introduction

Solar radiation is the basic energy source for surface biological, physical and chemical processes
45 (vegetation photosynthesis, evapotranspiration, plant and crop growth, etc.) (Wang et al., 2015; Liang
et al., 2019). It plays an important role in surface energy balance, land-atmosphere interactions,
weather and climate change (Li et al., 1997; Wang and Dickinson, 2013; Huang et al., 2019).
Furthermore, it is the key input data for land surface process models, hydrological models and earth
system models (Pinker et al., 2005; Liang et al., 2010; Stephens et al., 2012; Letu et al., 2020).

50 The Tibetan Plateau (TP) covers an area of approximately 2.65 million square kilometers. It is
known as the "Roof of the World" and "the Third Pole of the Earth" because of its average altitude of
more than 4000 m (approximately 1/3 of the troposphere height) and extremely complex topography
(Qiu, 2008; Yao et al., 2012). In addition, the TP and its surrounding areas hold the largest number of
glaciers outside the polar regions (Yao et al., 2012). The Yangtze River, the Yellow River, the Indus
55 River and most major rivers in Asia originate from the TP, and thereby the TP is also called the "Asian
Water Tower" (Xu et al., 2008; Immerzeel et al., 2010). Therefore, the unique features of the TP make it
an important research object for global and regional energy and water circulation and is one of the most
sensitive regions in response to global climate and environmental change.

Due to its high altitude, low airmass and short path for solar radiation to reach its surface, the TP
60 receives a large amount of radiation (Yang et al., 2014; Ma et al., 2017). The analysis of existing
observation data shows that the solar radiation heating effect of the TP is obviously stronger than that
of surrounding areas. Even the measured downwelling shortwave radiation (DSR) exceeds the solar

constant that occurs frequently (Tanaka et al., 2001; Yang et al., 2006b; Yang et al., 2008). As a result, the TP can generate an intense surface heating field, which drives atmospheric circulation, regulates the formation and development of the East Asian monsoon, and exerts an important impact on global weather processes and climate change (Hong et al., 2012; Wu et al., 2012; Zhao et al., 2018; Zhao et al., 2019b). Radiation-related changes to the environment become more severe in the case of global warming, such as significant snow melt, glacier retreat and permafrost thawing (Piao et al., 2010; Yang et al., 2010b; Kuang and Jiao, 2016). In turn, these processes may pose a threat to engineering constructions such as the Qinghai-Tibetan highway and railway (Chen et al., 2006; Yang et al., 2010a). Meanwhile, in the context of carbon neutrality, DSR has become not only a vital source of energy for local residents, but also an indispensable part of photovoltaic energy technologies (Zhang et al., 2017; Huang et al., 2022; Yang et al., 2022). Consequently, reliable DSR estimation over the TP is of great value for many studies and related practical applications.

For many years, in situ measurements, numerical modeling, and satellite remote sensing have been three effective ways to obtain DSR (Liang et al., 2019). In situ measurements are the most direct and reliable way to obtain DSR data with high accuracy and high temporal resolution. However, due to the high maintenance cost of field instruments, DSR observations are available at a smaller number of stations compared to other routine meteorological variables, such as air temperature, pressure and humidity, especially in areas with harsh climate conditions (e.g., Antarctica, the Arctic and the TP). In situ measurements of DSR in these regions are not only sparse but also unevenly distributed. It is therefore not enough to characterize the distribution pattern of DSR at a large spatial scale. Numerical models can provide spatiotemporally continuous DSR data at regional and global scales. However, the spatial resolution is relatively coarse (Decker et al., 2012). The accuracy is limited due to the uncertainties of models in simulating or predicting cloud quantities. In contrast, satellite remote sensing technology has certain advantages in estimating DSR with high spatial resolution over a large spatial coverage. The sensors aboard satellites can dynamically monitor the evolution and spatial distribution of clouds and capture a large amount of information about the atmosphere and underlying surface.

During the past few decades, various satellite-based methods for estimating DSR have been developed, which can be roughly divided into two categories: statistical methods and methods based on radiative transfer processes (Sengupta et al., 2018; Huang et al., 2019; Letu et al., 2020). The statistical

methods used to estimate DSR construct the functional relationship between satellite measurements and in situ observations. Traditional empirical methods are simple to operate by applying statistical regression (Masuda et al., 1995; Li et al., 1997). However, the empirical model may work at the local scale but needs recalibration over different regions. Artificial intelligence models, which can estimate DSR by building nonlinear relationships between satellite signals and ground-based DSR, have become a new trend to estimate radiation flux (Lu et al., 2011; Qin et al., 2011; Wei et al., 2019; Ma et al., 2020a). However, owing to an insufficient physical basis, the calculation accuracy of such methods depends largely on the selection of training data, and consequently, their generalizability is limited. In addition, the artificial intelligence model usually needs a large number of samples to train the model. Therefore, due to insufficient ground-based observations, this method is not easy to apply in the TP (Yang et al., 2010a; Zhang et al., 2015). The look-up table (LUT) and physical parameterization method (Pinker and Laszlo, 1992; Bisht et al., 2005; Liang et al., 2006; Lu et al., 2010; Xie et al., 2016; Tang et al., 2019) are two typical methods based on the radiation transfer process and have been widely used to estimate DSR from satellite data. Since LUT is a close approximation to the complicated radiative transfer model (RTM), a large number of parameters are needed as inputs, such as cloud, aerosol and atmospheric parameters, to obtain higher estimation accuracy. However, the data volume in the LUT will be greatly increased, which will further reduce the estimation efficiency of DSR. At the same time, it is usually necessary to encrypt the discrete calculation results by means of complex interpolation algorithms (Letu et al., 2020), which in turn will lead to a computational load. Alternatively, the physical parameterization method can alleviate the computational burden by parameterizing the complex process in RTM while maintaining sufficient estimation accuracy.

To date, the DSR parameterization scheme under clear-sky conditions has been quite mature (Bisht et al., 2005; Gueymard, 2012; Hwang et al., 2012). However, since optical remote sensing is greatly affected by clouds, it is still a problem to be solved to estimate DSR efficiently and accurately under all-sky conditions (Li et al., 1995; Li et al., 1997; Huang et al., 2019; Zhong et al., 2019; Letu et al., 2020). Although some studies have proposed parameterization schemes for cloudy-sky conditions, the current schemes still have some defects. In the presence of clouds, cloud-sky parameterization, which only considers cloud fraction and cloud optical thickness, is usually coupled into clear-sky models in a simple and arbitrary manner (Niemela et al., 2001; Bisht and Bras, 2010). Second, some

parameterization schemes did not consider the DSR attenuation caused by clouds carefully enough. Generally, only the single scattering of clouds was considered, and the multiple scattering effect of clouds was ignored (Huang et al., 2018; Huang et al., 2020).

Due to the high elevation and complex terrain of the TP, the impact of terrain on DSR should be taken into account. Tovar et al. (1995) found that there is no obvious correlation between the spatial variation in radiation in mountainous areas and interstation distance, but it varies with the altitude difference. Therefore, the DSR in mountainous areas cannot be estimated simply by interpolation of adjacent observation values. Yang et al. (2006b) pointed out that GEWEX-SRB v2.5 greatly underestimated the DSR on the TP due to ignoring the influence of surface elevation. Olson and Rupper (2019) reported that the deviation of the surface radiation budget could exceed 40 W m^{-2} during the summer melting season in the high-mountain Asia area. In addition, the coarse spatial resolution of most existing DSR products is prone to cause uncertainties in rugged areas such as the TP. Currently, the spatial resolution and accuracy of most existing DSR products cannot meet the requirements of energy and water cycle studies over the TP (Zhong et al., 2019a; Wang et al., 2021; Zhang et al., 2022). Therefore, all-sky DSR products with fine spatial resolution and high accuracy over the entire TP are still lacking.

In general, some existing DSR estimation methods are still not applicable to the TP due to its highly variable terrain, high elevation, and unique climatic conditions. Therefore, an effective method to estimate the DSR of the entire TP under all-sky conditions is urgently needed. In this study, an improved parameterization scheme is proposed, and the derived DSR is validated by in situ measurements and compared with various existing DSR products. Then, the spatiotemporal distribution of the estimated DSR is presented, and the improvement brought by considering the multiple scattering effect of clouds and topographic factors is discussed. The paper is organized as follows: Section 2 introduces the input data and validation data. Section 3 introduces the improved parameterization method. Section 4 presents the results and discussion. The main conclusions are given in Section 5.

2 Data

2.1 Input data

The basic information of the meteorological forcing data and satellite datasets are listed in Table 1. The

China Meteorological Forcing Dataset (CMFD) has a temporal resolution of 3 hours and a horizontal
150 spatial resolution of 0.1°. It has been widely used by the scientific community due to its high resolution
and quality. These forcing data were produced by combining routine meteorological observations of the
China Meteorological Administration (CMA), Princeton reanalysis datasets, the Global Land Data
Assimilation System (GLDAS), the GEWEX Surface Radiation Budget (GEWEX-SRB) and the
Tropical Rainfall Measuring Mission (TRMM) satellite (He et al., 2020). The surface air pressure (Pa),
155 air temperature (K) and specific humidity (kg kg^{-1}) are used for DSR estimation.

The satellite data come from MODIS, OMI and ASTER. The inputs for the parameterization
scheme include (1) the cloud phase, cloud water path (CWP), cloud effective radius (CER) (MODIS
cloud product MOD06_L2), (2) aerosol optical depth (AOD) (MODIS aerosol products MOD04_L2),
(3) ground surface albedo (MODIS Combined Land Albedo Product MCD43C3), (4) geolocation
160 information (MOD03), (5) total ozone column amount (OMTO3e), and (6) 30-m ASTER digital
elevation model.

The MODIS combined Dark Target and Deep Blue AOD at 0.55 μm for land and ocean were used
to derive the aerosol Ångström turbidity coefficients (Kim, 2004; Yang et al., 2006a; Huang et al.,
2018). The actual surface albedo is derived with the shortwave black sky albedo (BSA) and white sky
165 albedo (WSA) from the albedo product (Schaaf et al., 2002; Pinty et al., 2005). All MODIS product
versions mentioned above are in collection 6. The OMI science team created the OMTO3e product by
selecting the best pixel data from the high-quality filtered level-2 total column ozone data (Ahn et al.,
2008).

It should be noted that in operational applications, many parameters may not be available,
170 especially in areas with extreme climatic conditions, such as the TP. Therefore, the "gap-filling"
procedure should be carried out first, as in most studies. For aerosols, the invalid retrievals would be
substituted using the Level-3 MODIS global daily and monthly climatological products (Qin et al.,
2015; Huang et al., 2016a; Li et al., 2022). For the ozone column amount and surface albedo, the
unavailable retrievals were substituted using the nearest valid retrievals (Huang et al., 2018; Tang et al.,
175 2019; Zhong et al., 2019b). The spatial resolutions of MODIS aerosol and albedo data are 10 km and 5
km, respectively. The spatial resolutions of ozone and DEM data are 25 km and 30 m, respectively. To
obtain the DSR at the 1 km spatial scale, these data were resampled to 1 km.

Table 1. Overview of the meteorological forcing and satellite datasets used in this study.

Data sources	Product name	Variable	Spatial resolution	Temporal extent
CMFD	-	Temperature	0.1° x 0.1°	1979 to 2018
		Pressure		
		Specific humidity		
		Cloud phase		
MODIS	MOD06_L2	Cloud water path	1 km	2000 to present
		Cloud effective radius		
	MOD04_L2	Aerosol optical depth	10 km	
	MCD43C3	Black-Sky albedo	5 km	
		White-Sky albedo		
		MOD03	Latitude	
		Longitude		
ASTER	AST14DEM	DEM	30 m	2000 to present
OMI	OMT03e	Total column ozone	0.25° x 0.25°	2004 to present

180 2.2 In situ observation stations

The distributions of the in situ observation stations are marked in Fig. 1, and their basic information is listed in Table 2. In this study, in situ DSR observations used to validate the accuracy of the improved parameterization scheme were extracted from 12 stations over the TP. A variety of elevations, climates, and land cover types are included in these validation stations. Among them, six stations are obtained

185 from the Tibetan Observation and Research Platform (TORP) project (Ma et al., 2008), including BJ, QOMS, SETORS, NADORS, MAWORS and NAMORS stations. These six stations composed an integrated high-elevation and cold-region observation network. More detailed descriptions of these six stations are described by Ma et al. (2020b). The Xidatan (XDT) monitoring station representing the characteristics of discontinuous and warm permafrost is located along the northern permafrost

190 boundary of the TP. The Tanggula (TGL) monitoring station is located in the hinterland of the TP and is characterized by a continuous and cold permafrost zone (Yao et al., 2011; Zhao et al., 2021). There are two stations in the Ngoring Lake basin, which is located in the Yellow River source area east of the TP (Li et al., 2017). One grassland station (NLGS) is located on a flat surface, and the other observation station (NLTS) is located on the lakeside beside the lakeshore tower station (Li et al., 2020; Li et al.,

195 2021). The in situ data of D105 and NPAM come from the Coordinated Enhanced Observing Period Asia-Australia Monsoon Project (CAMP) on the Tibetan Plateau (CAMP/Tibet) (Ma et al., 2009;

Zhong et al., 2010; Ma et al., 2014). Plausible value checks, time consistency checks and internal consistency checks were applied to ensure the accuracy and reliability of the observations. The original sampling data with high frequency were uniformly processed into 30 min and hourly average data by data loggers (e.g., CR3000, CR1000) (Campbell Sci., USA). To retain the observations in their original form as much as possible, no further postprocessing processes are taken, except for replacing outliers with missing values (NaN). Meanwhile, periodic inspection, maintenance and calibration are carried out by professional engineers at all stations.

Table 2. Basic information for the in situ observation stations over the Tibetan Plateau.

Site	Lat(°N)	Lon(°E)	Altitude(m)	Land cover	Instrument	Frequency
BJ	31.37	91.90	4509	Alpine meadow	CM21, Kipp & Zonen	1 h
D105	33.06	91.93	5039	Alpine sparse grassland	CM21, Kipp & Zonen	1 h
NPAM	31.93	91.71	4620	Alpine meadow and grassy marshland	CM21, Kipp & Zonen	1 h
QOMS	28.36	86.95	4298	Gravel and sparse meadow	CNR1, Kipp & Zonen	1 h
SETORS	29.77	94.73	3327	Alpine meadow	CNR1, Kipp & Zonen	1 h
MAWORS	38.41	75.05	3668	Alpine desert	NR01, Kipp & Zonen	1 h
NADORS	33.39	79.70	4270	Alpine desert	NR01, Kipp & Zonen	1 h
NAMORS	30.77	90.98	4730	Alpine steppe	NR01, Vaisala	1 h
NLGS	34.91	97.55	4280	Flat Grassland	CNR4, Kipp & Zonen	0.5 h
NLTS	34.91	97.57	4275	Water	CNR4, Kipp & Zonen	0.5 h
XDT	35.72	94.13	4538	Alpine meadow	CM3, Kipp & Zonen	0.5 h
TGL	33.07	91.94	5100	Alpine sparse meadow	CM3, Kipp & Zonen	0.5 h

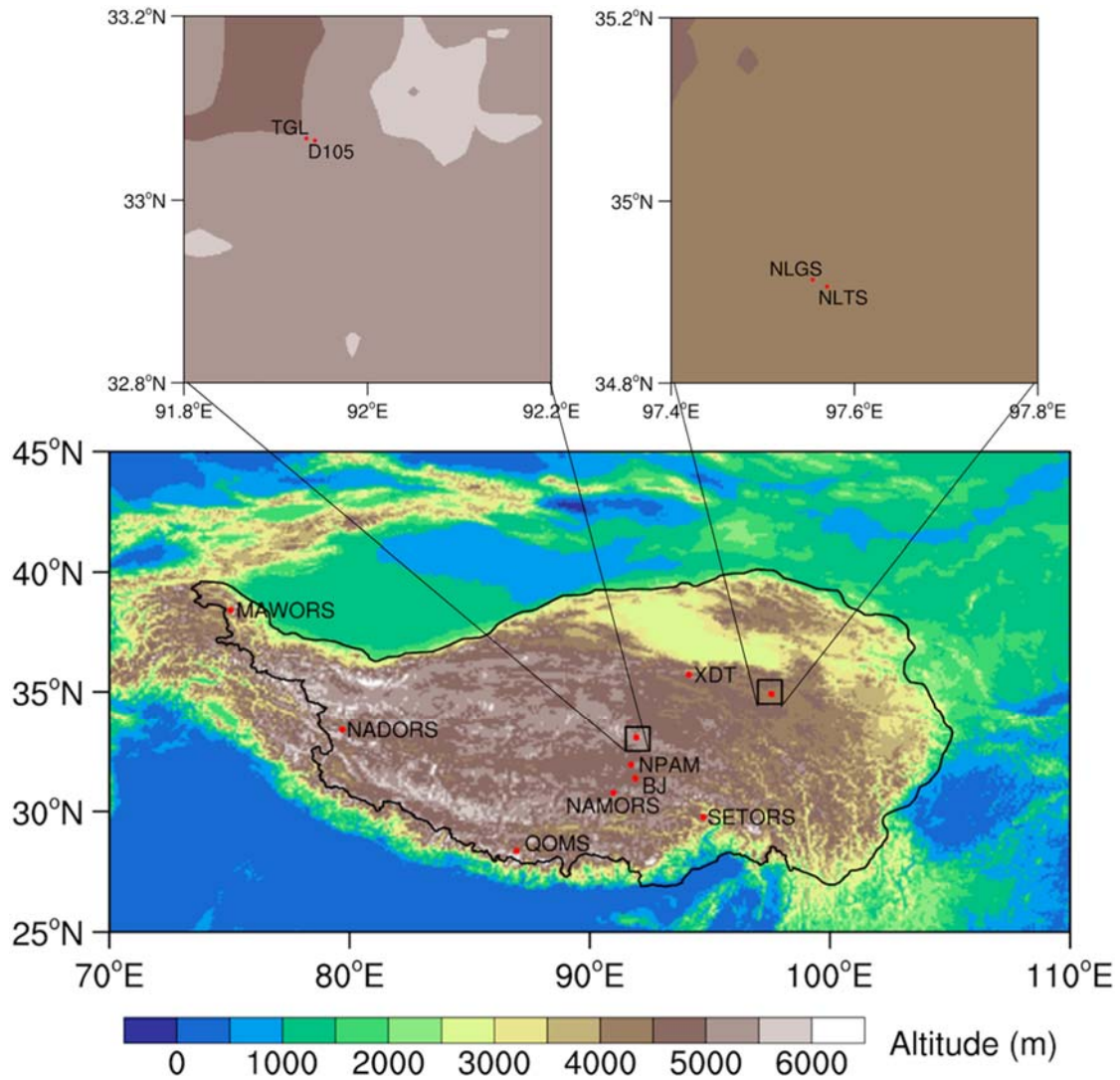


Figure 1. Locations of the twelve in situ observation stations over the TP. The legend of the color map indicates the elevation above mean sea level in meters.

3 Methodology

210 The effects caused by ozone, aerosol, water vapor, Rayleigh scattering, permanent gases, clouds and terrain are comprehensively taken into account in the improved parameterization scheme. More importantly, the DSR varies with altitude, surface slope and aspect, and the multiple actions of cloud and topography factors on DSR have been neglected in many previous studies. The all-sky DSR estimation method is divided into two groups, one for clear-sky conditions and the other for cloudy-sky

215 conditions. The main steps of the method and related key variables are shown in Fig. 2.

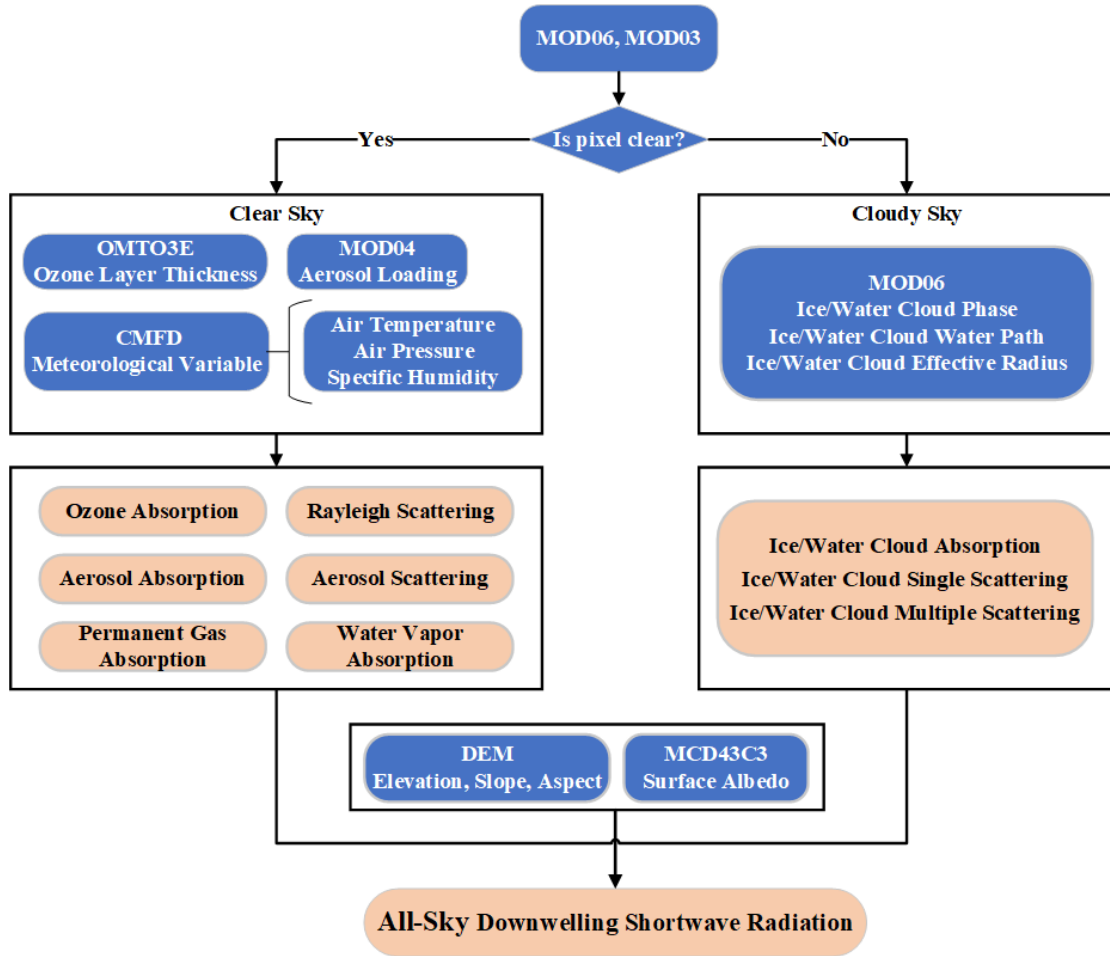


Figure 2. Flowchart for estimating all-sky DSR.

3.1 Clear-Sky Scheme

The DSR under clear-sky conditions (DSR_{clr}) can be calculated as the sum of three components: direct
 220 (beam) radiation ($S_{b,clr}$), diffuse radiation ($S_{d,clr}$), and reflected insolation from the surrounding terrain
 ($S_{r,clr}$).

$$DSR_{clr} = S_{b,clr} + S_{d,clr} + S_{r,clr} = S_0(\tau_{b,clr} + \tau_{d,clr} + \tau_{r,clr}), \quad (1)$$

where S_0 denotes the horizontal extraterrestrial solar insolation, which may slightly change with the
 earth-sun distance throughout the year. In addition, $\tau_{b,clr}$ is the direct radiative transmittance; $\tau_{d,clr}$ is
 225 the diffuse radiative transmittance; and $\tau_{r,clr}$ is the reflectance radiative transmittance.

3.2 Cloud-Sky Scheme

DSR under cloudy-sky conditions (DSR_{cld}) can be divided into four items as follows:

$$DSR_{cld} = S_{b,cld} + S_{d,cld} + S_{am,cld} + S_{r,cld}$$

$$= S_0\tau_{b,cld} + S_0\tau_{d,cld} + S_0(\tau_{b,cld} + \tau_{d,cld})\frac{\rho_{a,cld}\rho_g}{1-\rho_{a,cld}\rho_g} + S_0\tau_{r,cld}, \quad (2)$$

230 where the first, second and fourth items are the direct solar irradiance ($S_{b,cld}$), diffuse solar irradiance ($S_{d,cld}$), and reflected solar irradiance ($S_{r,cld}$) under cloudy conditions, respectively. The third item is the ambient solar irradiance caused by the interactions between the surface and atmosphere ($S_{am,cld}$). $\tau_{b,cld}$ is the direct radiative transmittance; $\tau_{d,cld}$ is the diffuse radiative transmittance; $\tau_{r,cld}$ is the reflectance radiative transmittance; and $\rho_{a,cld}$ is the atmosphere hemispherical albedo under
235 cloudy-sky conditions. ρ_g is the ground surface albedo.

The variations in elevation, slope and aspect of the land surface are considered for the above radiative transmittance. A detailed description of $\tau_{b,clr}$, $\tau_{d,clr}$, $\tau_{r,clr}$, $\tau_{b,cld}$, $\tau_{d,cld}$, $\tau_{r,cld}$, $\rho_{a,cld}$ and ρ_g is presented in Appendix A.

4 Results and Discussions

240 Considering the integrity and temporal continuity of the available data, the data of the BJ, D105, NPAM and SETORS stations in 2008, the data of the QOMS station in 2008 and 2015, and the data of the remaining seven stations in 2015 are used for validation. To ensure the reliability of the validation, first, the outliers in the ground-based observations were removed by considering the valid range and time continuity. Then, the hourly data were smoothed to 30 minutes to match the satellite overpass time
245 and the station observation time (Huang et al., 2016b). The root-mean-square error (RMSE), mean bias (MB), mean absolute error (MAE) and Pearson correlation coefficient (R) are used to evaluate the performance of the radiation parameterization scheme.

4.1 Validation against in situ measurements

As shown in Fig. 3a and 3b, at the instantaneous scale, the RMSE and R of the 1 km DSR under
250 clear sky are 105.34 W m⁻² and 0.76, respectively, while those of the 1 km all-sky DSR are 158.19 W m⁻² and 0.70, respectively. The validation results of this study are not as good as those in other plain areas, where RMSE and R are usually approximately 60 W m⁻² and 0.9 under clear skies, while those of all-sky conditions are approximately 100 W m⁻² and 0.9, respectively. Nevertheless, considering the unique climate characteristics of the TP and compared with the existing DSR products and algorithms
255 (see Section 4.2 and Section 4.4 for details), the accuracy of the results is within an acceptable range.

Roupioz et al. (2016) estimated all-sky solar radiation at an instantaneous timescale based on MODIS products, but the retrievals were validated using only BJ, QOMS and NAMORS stations. In their study, the RMSE, MB and R of BJ station were 225.5 W m^{-2} , 120.1 W m^{-2} and 0.51, respectively; the RMSE, MB and R of QOMS station were 117.1 W m^{-2} , 13.0 W m^{-2} and 0.74, respectively; and the RMSE, MB and R of NAMORS station were 203.5 W m^{-2} , 39.5 W m^{-2} and 0.55, respectively. Table 3 shows that the accuracy of our DSR estimation is better than Roupioz's retrievals.

Representativeness errors of point-scale measurements can affect the validation results of instantaneous DSR estimations to some extent. The insufficient spatial representation of point-scale observations can be partly compensated by lowering their temporal resolution (Hakuba et al., 2013; Huang et al., 2016b). Therefore, the DSR estimation results were also validated at ten-day and monthly timescales. It is upscaled to ten-day and monthly timescales via averaging by instantaneous values. There are three 10-day periods within 1 month, which can be defined as follows: from the first to the 10th, from the 11th to the 20th, and from the 21st to the end of every month. Obviously, the estimation of DSR at a longer timescale shows more reasonable agreement with the in situ measurements compared with the instantaneous DSR estimations (Fig. 3c and Fig. 3d).

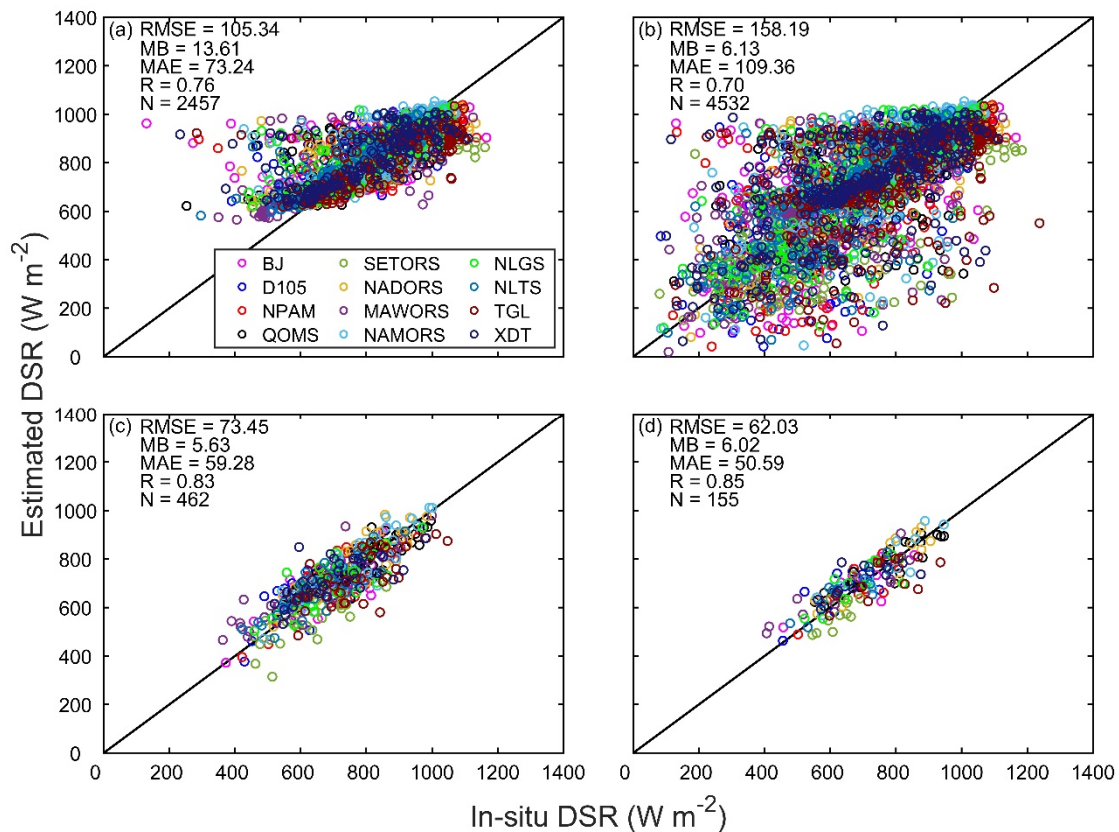


Figure 3. Validation results for the estimated DSR at (a and b) instantaneous scale, (c) ten-day scale and (d) monthly scale.

monthly scale. Scatter plots (a) and (b) show the validation results of instantaneous DSR under clear sky and all-sky conditions, respectively. N indicates the number of points. The legend with different colors denotes the twelve stations involved in the validation. The units of RMSE, MB and MAE are $W m^{-2}$.

The corresponding statistical indices for the twelve stations in this study are listed in Table 3. Since there is usually a distinctness between DSR estimation under clear-sky and cloudy-sky conditions, the statistics of specific stations are always related to the overall cloud fraction. Therefore, the proportion of cloud cover days (CCD) at each station is also listed in the table. Zhong et al. (2019b) estimated all-sky solar radiation on a ten-day timescale based on MODIS products over the TP, while their method needed to obtain ground-based measurements in advance for local calibration. We find that compared to the statistics presented at the D105, QOMS, and SETORS stations, the accuracies of our method are on average slightly higher.

As illustrated in Table 3, the best validation results occurred at the QOMS station, showing the lowest RMSE, the MB of a smaller absolute value, and the higher R, due to the extremely low CCD over there (~19.83%), whereas the poorer performance occurred at the SETORS and TGL stations, according to the validation results on various time scales. The SETORS station is located in the valley near the southeastern TP, surrounded by dense vegetation (mainly evergreen needle-leaved trees and alpine meadows) and is close to the southern water vapor transport channel. Accordingly, many precipitation events occur here, with a maximum CCD (~72.85%) among the twelve sites. The TGL station lies on the north side of the Tanggula Mountains, surrounded by numerous glaciers and deep snow cover, which can persist for many days (Xu et al., 2017; Zhou et al., 2018). Because the snow/ice cover beneath the clouds is difficult to identify from satellite signals, there is great uncertainty in the corresponding retrievals of cloud microphysical parameters, which may lead to low accuracy of the estimation results. In addition, previous studies have shown that snow cover will result in the underestimation of DSR (Pinker et al., 2007; Huang et al., 2016a), which is also indicated by the large negative MB of the TGL site compared with other stations.

Table 3. Summary statistics of the validation results for each station on different timescales.

Site	Instantaneous timescale				Ten-day timescale				Monthly timescale				CCD
	RMSE ($W m^{-2}$)	MB ($W m^{-2}$)	R	N	RMSE ($W m^{-2}$)	MB ($W m^{-2}$)	R	N	RMSE ($W m^{-2}$)	MB ($W m^{-2}$)	R	N	
BJ	179.44	11.41	0.66	359	66.20	13.91	0.84	36	56.01	14.54	0.81	12	49.58%
D105	162.87	32.47	0.67	359	76.69	33.23	0.73	36	67.43	33.80	0.73	12	54.02%

NPAM	177.57	-3.90	0.63	358	67.63	-4.28	0.82	36	51.90	-3.75	0.82	12	53.46%
QOMS	112.33	5.04	0.74	689	56.49	6.38	0.90	69	49.76	6.41	0.91	23	19.83%
SETORS	183.33	-49.51	0.67	302	94.17	-49.48	0.67	33	64.89	-44.04	0.74	12	72.85%
MAWORS	167.41	28.51	0.71	350	83.27	27.08	0.90	36	72.94	27.32	0.92	12	55.62%
NADORS	129.88	19.48	0.78	318	66.20	17.59	0.89	36	58.30	18.20	0.90	12	35.07%
NAMORS	150.62	18.30	0.72	342	65.60	13.66	0.88	36	55.92	13.42	0.89	12	40.27%
NLGS	141.53	11.26	0.77	365	66.51	10.81	0.81	36	56.48	11.02	0.80	12	46.58%
NLTS	136.29	24.63	0.79	360	62.80	22.01	0.86	36	51.55	23.81	0.87	12	59.45%
XDT	183.08	17.84	0.63	365	81.41	17.95	0.72	36	70.48	18.02	0.70	12	51.23%
TGL	188.98	-46.64	0.58	365	97.70	-46.52	0.72	36	87.80	-46.92	0.66	12	45.63%

300 4.2 Comparison among different DSR products

To further evaluate the reliability of our DSR estimates, several existing widely used DSR products were selected for comparison based on the same in situ observations used in Section 4.1. Among these products, there are remotely sensed and reanalysis DSR products, namely, Clouds and the Earth's Radiant Energy System Synoptic (CERES_SYN) surface fluxes (Loeb et al., 2013), Global Energy and Water Exchanges Surface Radiation Budget (GEWEX_SRB) datasets (Zhang et al., 2014), MODIS DSR product (MCD18A1) (Wang et al., 2020) and the fifth generation reanalysis (ERA5) from the European Centre for Medium-Range Weather Forecasts (ECMWF) (Hans et al., 2019). In addition, Letu et al. (2022) produced a high-resolution (5 km, 10 min) DSR dataset (short for "H-8_EAP" in our study) under all-sky conditions from 2016 to 2020 in the East Asia–Pacific region based on the next-generation geostationary satellite Himawari-8/AHI, which was also selected for comparison. At present, the latest in situ data in this study are in 2016, and the Himawari-8 satellite cannot observe the western part of the TP. Therefore, six stations (BJ, QOMS, SETORS, NAMORS, NLGS and NLTS) in 2016 are selected for comparison with the H-8_EAP DSR dataset.

The spatial resolutions of MCD18A1 and ERA5 are 1 km and 25 km, respectively. CERES_SYN and GEWEX_SRB have a spatial resolution of 100 km. It is known that spatial mismatch may incur errors in the validation results, so our results at the original scale of 1 km were aggregated to the corresponding spatial resolution of the above products. The temporal resolution of MCD18A1 is instantaneous. GEWEX_SRB has a temporal resolution of 3 hours and ERA5 has a temporal resolution of 1 hour. CERES_SYN products have two temporal resolutions of 1 hour and 3 hours. The abovementioned DSR products and the estimated DSR of this study were temporally matched to 10:30

local time for mutual comparison (Zhong et al., 2019b).

Table 4. Comparison with existing DSR products on different timescales in terms of accuracy.

Product name	Instantaneous timescale			Ten-day timescale			Monthly timescale			Spatial resolution
	RMSE (W m ⁻²)	MB (W m ⁻²)	R	RMSE (W m ⁻²)	MB (W m ⁻²)	R	RMSE (W m ⁻²)	MB (W m ⁻²)	R	
MCD18A1	233.47	-76.43	0.60	147.04	-74.60	0.72	130.24	-74.17	0.74	1 km
This study	152.13	5.23	0.72	77.24	7.35	0.82	63.79	7.25	0.84	
H-8_EAP	197.89	-52.47	0.66	140.67	-57.07	0.67	125.70	-62.74	0.73	5 km
This study	140.54	23.64	0.77	82.67	21.54	0.78	71.48	14.97	0.81	
ERA5	165.67	-20.59	0.65	88.06	-21.44	0.82	74.19	-21.06	0.86	25 km
This study	135.11	15.67	0.77	75.01	15.24	0.83	67.12	15.75	0.83	
CERES_SYN_1h	146.64	-46.70	0.75	84.27	-47.93	0.86	73.25	-47.53	0.89	100 km
CERES_SYN_3h	160.50	-78.30	0.74	107.13	-79.48	0.85	98.67	-79.06	0.88	
GEWEX_SRB	194.45	-118.56	0.68	143.68	-119.71	0.80	135.54	-119.21	0.83	
This study	132.84	2.79	0.77	70.84	2.18	0.84	61.33	2.70	0.85	

As summarized in Table 4, the RMSE range of these DSR products is approximately 150~230 W m⁻² at the instantaneous scale. At the ten-day scale, the RMSE range is approximately 80~150 W m⁻². At the monthly scale, the RMSE range is approximately 70~130 W m⁻². The MB range of these DSR products is -120 ~ -20 W m⁻² at three temporal scales. These large spans of RMSE and MB indicate that the current DSR products still have great uncertainties over the TP. The RMSE ranges of this study at three temporal scales are 132~152, 70~82 and 61~71 W m⁻². The MB range of this study is 3 ~ 24 W m⁻² at three temporal scales. The estimates of this study show a smaller RMSE, lower absolute value MB and comparable R values at the corresponding spatial and temporal scales. This means that the derived DSR based on the proposed method performs better than other DSR products over the TP.

In addition, it is noted that the accuracies of all datasets have been appreciably improved with increasing timescale. This is because the 3D radiative transfer effects and complexity of clouds can be significantly reduced and the spatial representativeness of ground-based measurements can be significantly enhanced through temporal averaging (Huang et al., 2016b; Huang et al., 2016a). A phenomenon in which the RMSE of this study has been improved with incremental space scales at three time scales is also found, while the variations are relatively small at the ten-day and monthly scales. This may be because the time mismatch between satellite observations and surface measurements can be partly decreased by inherent averaging in the upscaling of spatial resolution

(Tang et al., 2019).

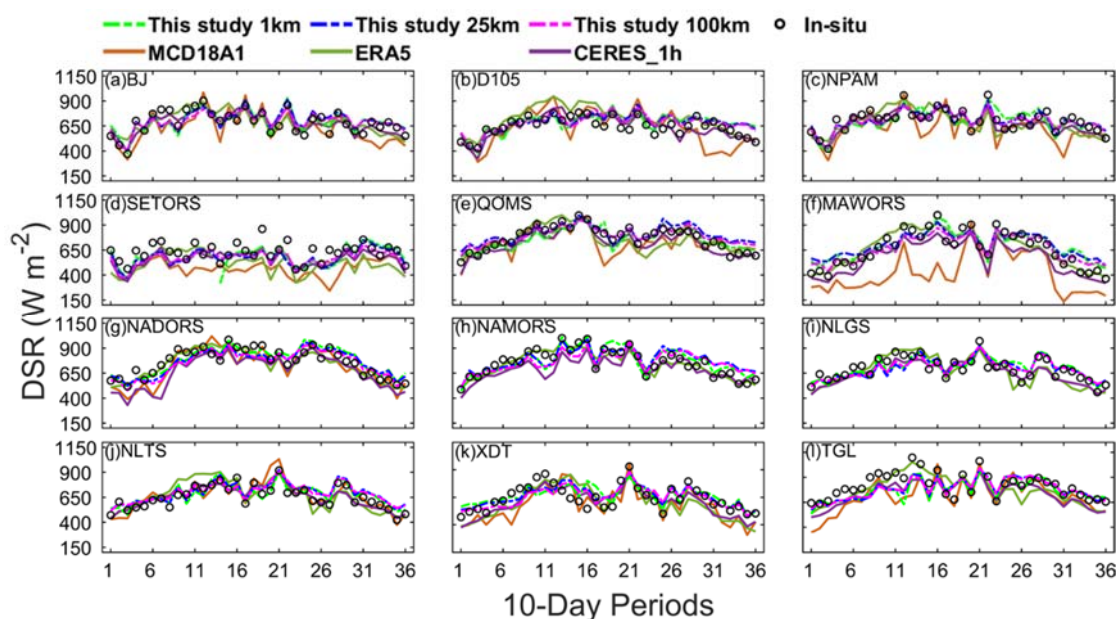


Figure 4. Intercomparison of time series of DSR among MCD18A1, ERA5, CERES_SYN_1 h, and this study at (a) BJ, (b) D105, (c) NPAM, (d) SETORS, (e) QOMS, (f) MAWORS, (g) NADORS, (h) NAMORS, (i) NLGS, (j) NLTS, (k) XDT, and (l) TGL stations on a ten-day timescale. The circle denotes in situ data.

345

DSR products with relatively high accuracy, which correspond to three spatial resolutions of 1 km, 25 km and 100 km, are selected for comparison with the estimated DSR in terms of temporal variation characteristics (Fig. 4). The time series of MCD18A1 at NAMORS and NLGS stations are not displayed because there are many missing values in MCD18A1 at these two stations. It can be seen that six selected DSR showed a quasi-convex shape in one year at all stations except SETORS. There are some fluctuations in DSR during the summer monsoon period due to the high frequency of clouds and precipitation. Almost all six selected DSRs showed relatively smooth variation at SETORS compared with other stations, which demonstrated a large variation with time. The dynamic range (defined as the difference between the maximum and the minimum in a year) of MCD18A1 is the largest, while ERA5, CERES_SYN_1 h and this study show similar dynamic ranges. Compared with other products, the derived DSR of this study is more consistent with the in situ observations at each station, and all show similar temporal change trends.

350

355

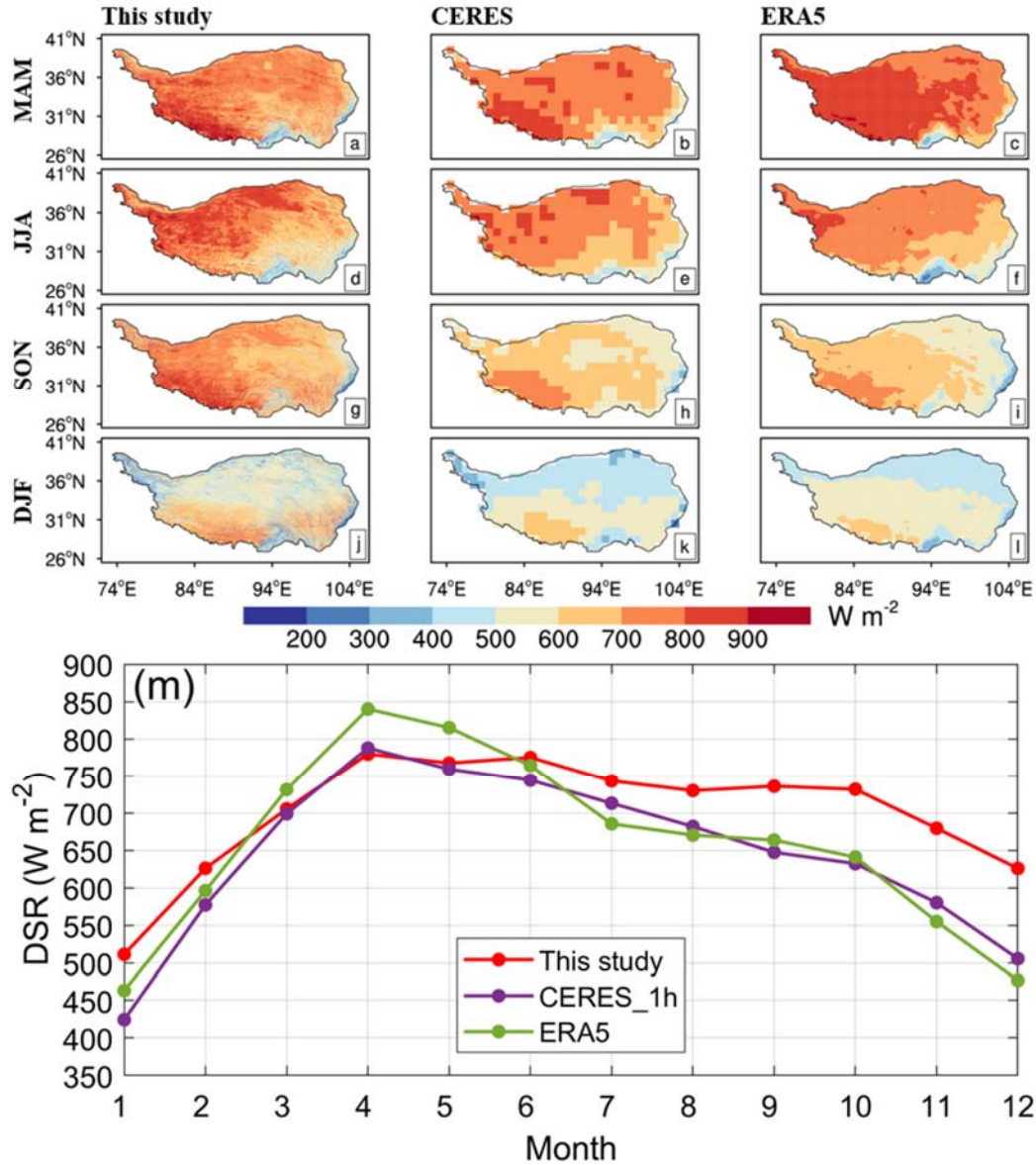
It should be noted that the six selected DSRs are not consistent with the in situ observations at the SETORS station, especially in the monsoon period in which obvious underestimation can be found. Cloud and precipitation occurrence frequencies generally reach peaks during the monsoon period over the TP. Compared with other regions of the TP, not only higher cloud amounts and frequencies but also

360

higher precipitation intensities and frequencies are found in the southeastern TP, where the SETORS station is located (Zhao et al., 2019a; Kukulies et al., 2020). Convective clouds appear most frequently over the TP near noon, and thus, the DSR may also partially come from the high diffuse radiation
365 caused by cloud scattering in addition to direct radiation (Fujinami et al., 2005; Li et al., 2008; Yang et al., 2010a). It is still difficult to reflect the 3D radiation effect of clouds, although this study has considered the scattering of clouds and thus may lead to underestimation of DSR. The microphysical processes of convective clouds generally include mixed-phase processes inside clouds (Fu et al., 2020). Nevertheless, only a single phase can be diagnosed by satellite-based cloud products, which may
370 significantly influence the retrieval accuracy of DSR (Platnick et al., 2003; Platnick et al., 2017). In addition, the SETORS station is flat with grass cover, while its surroundings are valley and dense evergreen needle-leaved trees. The domes of instruments are vulnerable to the contamination of precipitation, and further influence the spatial representativeness of in situ stations. Hence, some errors may be introduced due to the inadequate spatial representativeness of point-scale measurements
375 compared with the coarse resolution of satellite images.

4.3 Spatiotemporal variations in surface downward shortwave radiation

Based on the above analysis, CERES_SYN_1 h and ERA5 performed better than the other DSR products. To better investigate the spatiotemporal variations in the estimated DSR over the TP, the seasonal spatial distribution of DSR generated from CERES_SYN_1 h, ERA5 and this study in 2008
380 are collected and compared in Fig. 5. In general, the three mentioned DSR provide similar seasonal radiation patterns, i.e., the DSR values are higher in spring and summer and lower in autumn and winter. This phenomenon can also be found in the monthly mean DSR variation over the TP (Fig. 5m). The DSR increased from a minimum value in January to a maximum value in April. The formation of this pattern is primarily controlled by the north-south movement of the subsolar point.



385

Figure 5. Spatial distribution of DSR from this study (left), CERES_SYN_1 h (center), and ERA5 (right) for four seasons in 2008 over the TP. The first to fourth rows represent spring (March, April and May), summer (June, July and August), autumn (September, October and November), and winter (December, January and February), respectively. The bottom panel (m) shows the comparison of monthly temporal variation of spatial mean DSR estimates from this study, CERES_SYN_1 h, and ERA5 over the TP.

390

It should be pointed out that the radiation texture of this study is rather clear due to the higher resolution (1 km), and more details of DSR variations can be captured. The high values of DSR are mostly located in the western TP. This can be explained by the fact that the western TP, with arid and semiarid climate characteristics, has a higher altitude than the eastern TP, and thus, less radiation attenuation occurred. At the same time, the southern margin of the TP and the eastern margin of the TP near the Sichuan Basin are always low-value areas of DSR. The south edge of the TP is a water vapor

395

transport channel associated with the South Asian monsoon, and the frequencies of clouds and rainfall are high. The eastern edge of the TP near the Sichuan Basin has a very low altitude (~ 1800 m) and is often covered by stratiform clouds. Accordingly, strong solar radiation attenuation occurred in these two regions.

The difference among the three mentioned DSRs is also displayed in Fig. 5. The high value of DSR appears in the southwestern TP in spring, but the high value of ERA5 covers a large area and even extends to the Tanggula Mountains (Fig. 5a-c). The overall DSR pattern over the TP shows a decreasing trend from northwest to southeast in summer, but the high value in the Qaidam Basin is not found in ERA5 (Fig. 5d-f). In autumn, the high value of DSR is concentrated in the southwestern TP, showing a spatial pattern of high-west and low-east (Fig. 5g-i). In winter, the DSR reaches the minimum of the year and shows a spatial distribution of high-south and low-north over the TP (Fig. 5j-l). However, the DSR derived from this study is generally higher than that of the other two products. The monthly temporal variation in the spatial mean DSR over the TP also indicates a similar phenomenon (Fig. 5m). The spatial mean DSR of ERA5 is higher than those of the other two DSR products in spring, and the spatial mean DSR estimated in this study is higher than those of the other two radiation products in autumn and winter.

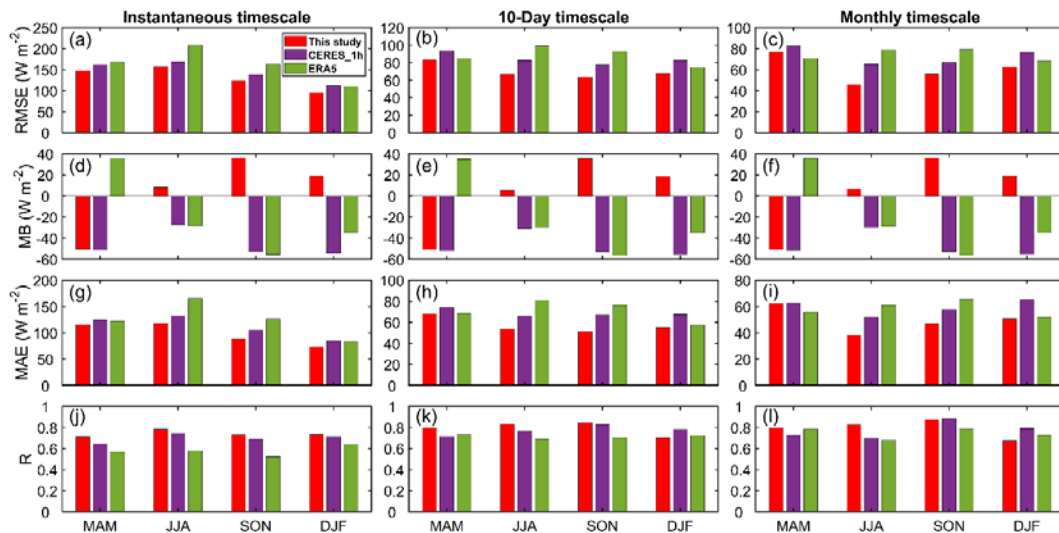


Figure 6. RMSE (a-c), MB (d-f), MAE (g-i) and R (j-l) between in situ observations and DSR estimates from this study (red bar), CERES_SYN_1 h (purple bar), and ERA5 (green bar) products in four seasons.

To further understand the difference between the three mentioned DSRs, the corresponding statistical indices for the four seasons are presented in Fig. 6. At all temporal scales in spring, ERA5 shows a positive bias, while the other two DSRs show a negative bias. In summer, autumn and winter,

the DSR estimated from this study shows positive bias, while the other two products show negative bias. This explains the above phenomenon. However, this study is significantly lower than the other two DSR products in terms of the absolute value of MB. Particularly, it can be clearly seen that in all seasons and temporal scales, not only in MB but also in terms of RMSE and MAE, this study shows the lowest values, and in terms of R, this study is comparable to or higher than the CERES_SYN_1 h and ERA5 products. Similar comparison and verification results can also be found in Table 4. In addition, the spatial distribution of this study is similar to that in a previous study by Zhong et al. (2019b). Therefore, it is not difficult to conclude from the above analysis that the DSR patterns of this study are reasonable enough, at least showing advantages over other products in terms of spatial resolution with relevant details.

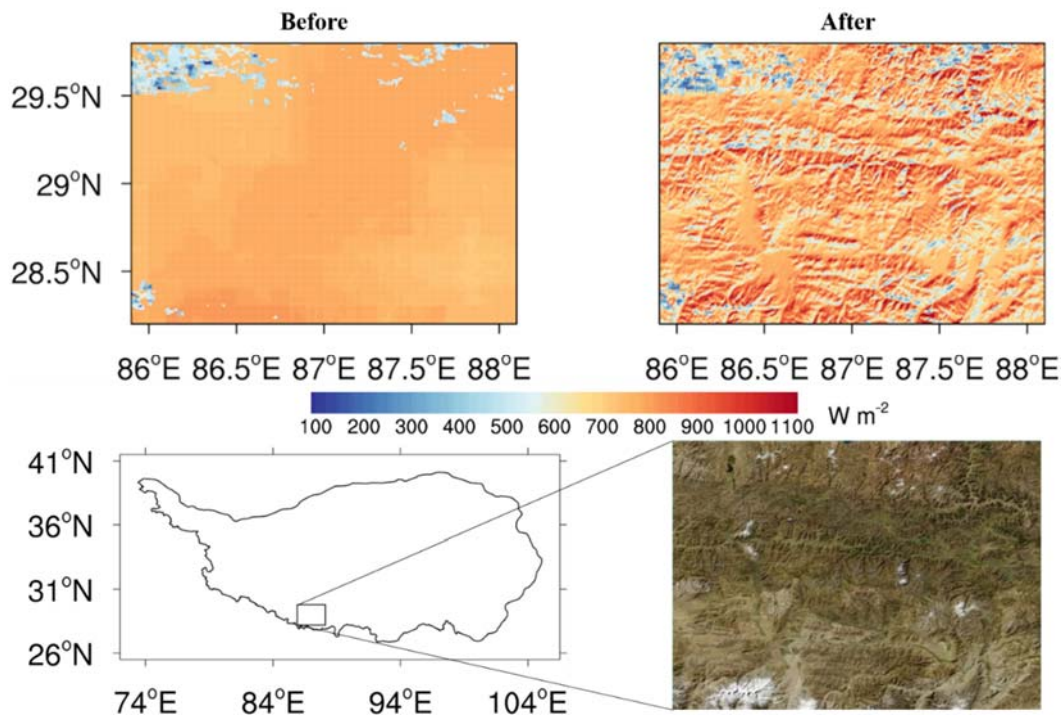
4.4 Evaluation of cloud multiscattering and topographic effects

To evaluate the effects of cloud multiscattering and complex topography, the accuracy of the DSR derived with and without considering terrain factors and cloud multiple scattering on different temporal scales were compared (Table 5). Here, four simple cases were designed. Both terrain factor and cloud multiple scattering are not included in Case 1; Case 2 only considers terrain factor, and Case 3 only considers cloud multiple scattering. Case 4 is the method adopted in this study; that is, both terrain factor and cloud multiple scattering are taken into account.

Table 5. Comparison between DSR estimation with and without considering cloud multiple scattering and terrain factors on different timescales in terms of accuracy.

		Case1	Case2	Case3	Case4
Instantaneous timescale	RMSE ($W m^{-2}$)	192.90	177.77	174.52	158.19
	MB ($W m^{-2}$)	57.23	12.04	51.58	6.13
	MAE ($W m^{-2}$)	132.48	119.71	121.74	109.36
	R	0.69	0.65	0.73	0.70
Ten-day timescale	RMSE ($W m^{-2}$)	96.54	80.79	87.53	73.45
	MB ($W m^{-2}$)	56.79	11.39	51.17	5.63
	MAE ($W m^{-2}$)	77.52	63.42	70.98	59.28
	R	0.87	0.81	0.89	0.83
Monthly timescale	RMSE ($W m^{-2}$)	84.50	66.45	77.44	62.03
	MB ($W m^{-2}$)	57.58	11.99	51.61	6.02
	MAE ($W m^{-2}$)	69.78	53.04	63.80	50.59
	R	0.90	0.83	0.91	0.85

As shown in Table 5, the RMSE of case 1 reaches nearly 200 W m^{-2} at the instantaneous scale, nearly 100 W m^{-2} at the ten-day scale, and more than 80 W m^{-2} at the monthly scale, all of which are the highest among the four cases. As mentioned earlier, the estimated DSR of the SETORS station is more vulnerable to clouds. The RMSE of the SETORS station is reduced by 15%-19% when cloud multiple scattering is considered. Hence, ignoring the multiple scattering of clouds may lead to large errors in the case of high cloud cover. The verification results are improved when multiple cloud scattering and varying topography are introduced, and the RMSE is reduced by 8%-25%. Obviously, Case 4 shows the lowest RMSE, MB, MAE, and comparable R values compared with the other three cases. This reflects that when estimating DSR under all-sky conditions over the TP, the effects of terrain and cloud multiscattering cannot be simply ignored.



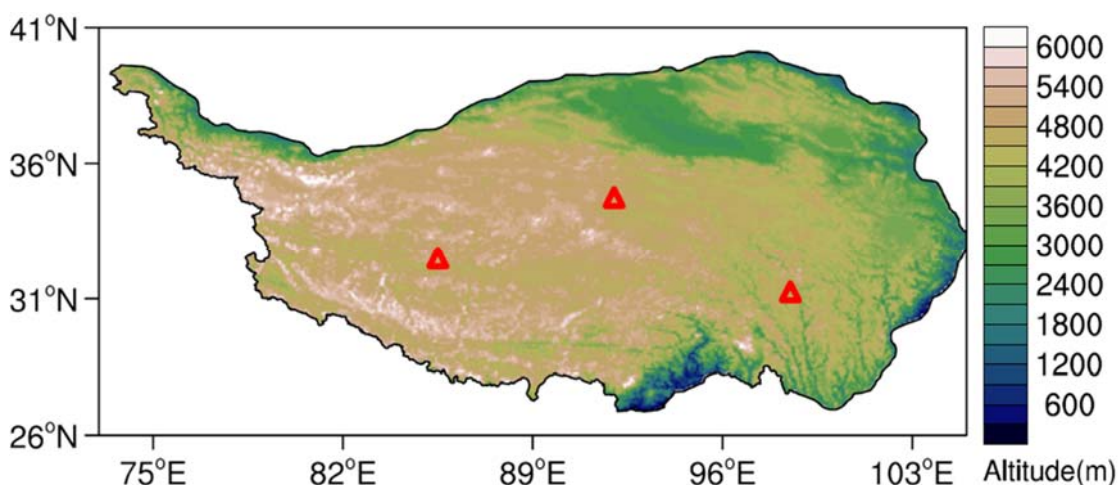
450 **Figure 7.** DSR estimated before terrain correction (left) and after terrain correction (right) over the TP at 10:30 LT on 10 January 2008.

To show the impact of varying topography on DSR, the spatial DSR pattern in a subarea of the TP before and after terrain correction is shown under relatively clear-sky conditions (Fig. 7). Before terrain correction, the value of DSR is uniform, and the spatial texture is relatively smooth. The majority of the selected areas show relatively fixed values ($\sim 750 \text{ W m}^{-2}$), except for the parts covered by clouds, which show obviously low values. In contrast, the DSR values show high spatial dynamics, and it is

easy to identify some subtle changes. The spatial gradient of DSR on the sunny and shady slope hillsides is obvious, and the higher parts receive more solar radiation. This is consistent with the surface features shown by the satellite images in the lower right corner.

460 4.5 Sensitivity analysis

The accuracy of the parameterization scheme depends on the quality of the input data to some extent. To further understand the effect of uncertainties in input variables on the accuracy of the DSR retrieval scheme, sensitivity analysis of the DSR to input variables is conducted (Fig. 9 and Fig. 10). As shown in Fig. 8, three points located in the west, north central, and southeast of the TP are randomly selected for sensitivity tests. The average of each input variable (including air temperature T_{air} , air pressure P_{air} , specific humidity SH, ozone layer thickness, aerosol optical depth AOD, surface albedo, cloud effective radius CER and cloud water path CWP) for three randomly selected points is selected as the default value.



470 **Figure 8.** Locations of the three points (marked by red triangles) used to carry out sensitivity tests of the input data. The legend of the color map indicates the elevation above mean sea level in meters.

As shown in Fig. 9 and Fig. 10, in terms of changing trend and range, DSR has different responses to fluctuations of each input variable under different sky conditions. The sensitivity test results show that the DSR exhibits a positive correlation with P_{air} and ozone layer thickness and a negative correlation with T_{air} under both clear and cloudy conditions, with a nearly linear relationship (Fig. 9a, b, d and Fig. 10a, b, d). The DSR exhibits a negative correlation with SH and AOD with a nonlinear relationship under both clear and cloudy conditions (Fig. 9c,e and Fig. 10c,e). In addition, the DSR exhibits a positive correlation with CER and a nonlinear negative correlation with CWP under cloudy

sky conditions (Fig. 10g and h). However, the DSR exhibits a linear positive correlation with surface
 480 albedo under clear sky conditions, while it displays a nonlinear positive correlation under cloudy sky
 conditions (Fig. 9f and Fig. 10f). This phenomenon indicates that multiple scattering effects occur
 between the atmospheric medium (aerosols and clouds) and the land surface (Ma et al., 2020).

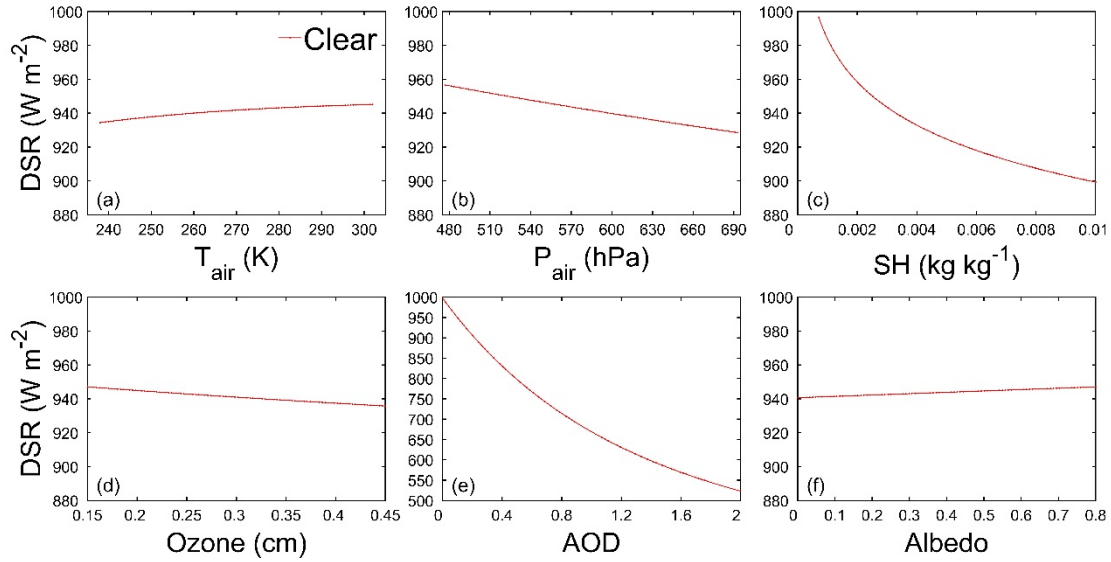


Figure 9. Sensitivity of DSR to (a) air temperature T_{air} , (b) air pressure P_{air} , (c) specific humidity SH, (d) ozone
 485 layer thickness, (e) aerosol optical depth AOD and (f) surface albedo under clear sky conditions.

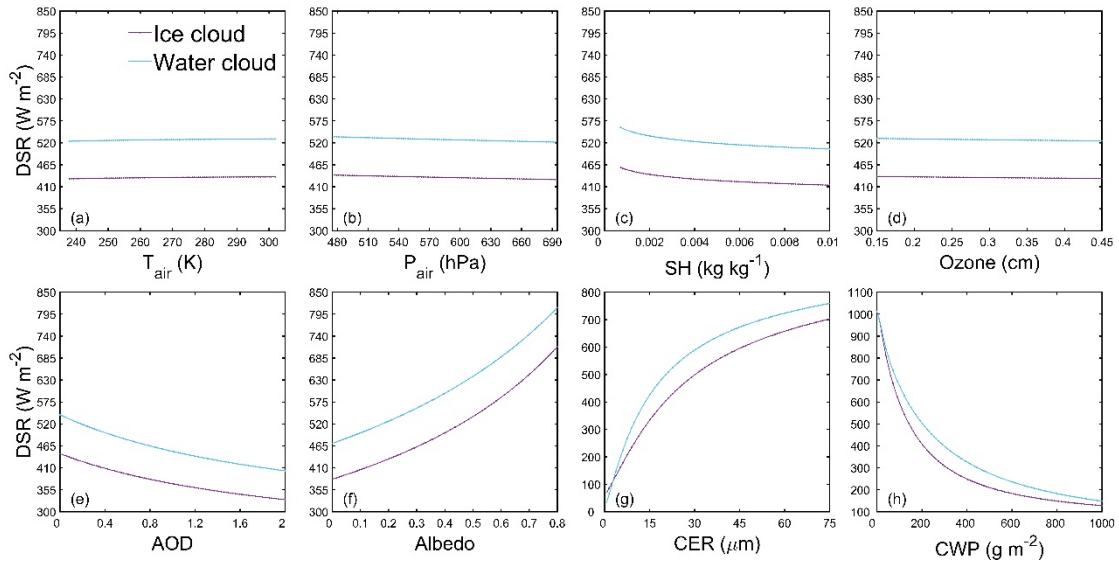


Figure 10. Sensitivity of DSR to (a) air temperature T_{air} , (b) air pressure P_{air} , (c) specific humidity SH, (d) ozone
 layer thickness, (e) aerosol optical depth AOD, (f) surface albedo, (g) cloud effective radius CER and (h) cloud
 water path CWP under cloudy sky conditions for ice clouds (purple line) and water clouds (blue line).

490 Moreover, the fluctuating range of input variables within one standard deviation (1σ) and the
 induced DSR fluctuation under different sky conditions are summarized in Table 6. Under clear sky
 conditions, the DSR is highly sensitive to AOD and SH and only slightly sensitive to other input

variables. The AOD and SH within 1σ correspond to ranges of approximately 0-0.23 and 0.0004-0.0047 kg kg^{-1} , respectively, which would lead to DSR fluctuating by approximately 100.6 W m^{-2} and 87.4 W m^{-2} , respectively. Other input variables only induce fluctuations in DSR smaller than 15 W m^{-2} . Under cloudy sky conditions, the DSR shows significant sensitivity to CWP and CER, moderate sensitivity to albedo, SH and AOD, and slight sensitivity to other input variables. The CWP within the 1σ range would lead to DSR fluctuating by approximately 768.1 W m^{-2} and 526.7 W m^{-2} for ice clouds and water clouds, respectively. The CER within the 1σ range would lead to DSR fluctuating by approximately 212.2 W m^{-2} and 202.3 W m^{-2} for ice clouds and water clouds, respectively. The magnitude of DSR fluctuations induced by the remaining input variables is much smaller than that caused by CWP and CER. In addition, the sensitivity of DSR to albedo is higher under cloudy sky conditions than under clear sky conditions, while the sensitivity of DSR to AOD and SH is lower under cloudy sky conditions than under clear sky conditions.

Table 6. Fluctuating range of input variables within one standard deviation (1σ) and the induced DSR fluctuation under clear sky and cloudy sky conditions.

Variables	Clear		Ice cloud		Water cloud	
	Ranges of variables within 1σ	DSR fluctuation range (W m^{-2})	Ranges of variables within 1σ	DSR fluctuation range (W m^{-2})	Ranges of variables within 1σ	DSR fluctuation range (W m^{-2})
	T_{air} (K)	264-282	2.6	263-282	1.3	271-288
P_{air} (hPa)	530-622	-12.0	537-633	-4.9	550-646	-5.7
SH (kg kg^{-1})	0.0004-0.0047	-87.4	0.0006-0.0059	-38.0	0.0035-0.0083	-17.34
Ozone (cm)	0.25-0.28	-1.3	0.25-0.30	-0.7	0.25-0.28	-0.6
AOD	0-0.23	-100.6	0.03-0.21	-19.7	0.06-0.23	-21.1
Albedo	0.09-0.32	1.8	0.08-0.35	82.9	0.06-0.29	65.7
CER (μm)	-	-	16.7-39.8	212.2	9.3-21.4	202.3
CWP (g m^{-2})	-	-	0-409.6	-768.1	29.8-351.1	-526.7

In general, the inputs of cloud parameters CWP and CER are crucial variables, and their sensitivities are consistently high. AOD, surface albedo and SH are of secondary importance, with moderate sensitivity. AOD and surface albedo are more sensitive to DSR estimation than SH. T_{air} , P_{air} and ozone layer thickness only have a slight sensitivity to DSR estimation, in which ozone layer thickness is the least sensitive. The sensitivity test results indicate that the uncertainties in the input data of cloud parameters, aerosol parameters, surface albedo, and water vapour content are important error sources in the estimation of DSR (Huang et al., 2020; Letu et al., 2020).

515 **5 Summary**

Various satellite-based methods for estimating DSR have been developed during the past few decades, but some of them rarely operate effectively over the TP due to its complex terrain, high elevation, and unique climatology. Current surface radiation products ignore the influence of topographic variability on the DSR by simply assuming that the surface is horizontal and uniform, resulting in unreliable estimations in rugged regions. Due to the complexity and heterogeneity of the underlying surface of the TP, it is indispensable to consider the topographic variability in the process of DSR estimation. However, few models take the terrain effect into account on the large spatial scale of the whole TP. Unlike aerosol scattering and Rayleigh scattering, multiple scattering plays an important role in DSR attenuations caused by clouds. However, radiative extinctions due to cloud multiscattering tend to be ignored in existing DSR estimation methods under cloudy-sky conditions.

Thus, an improved parameterization scheme for deriving DSR over the TP under all-sky conditions is proposed in this paper. Based on meteorological forcing data and satellite data, the effects caused by ozone, aerosol, water vapor, Rayleigh scattering, permanent gas, cloud single scattering, cloud multiple scattering and topography are comprehensively considered in the improved parameterization scheme. The estimated DSR was validated against in situ observations collected at 12 stations over the TP, which cover a variety of elevations, climates, and land cover types. The validation results on different temporal scales show that the derived DSR based on the developed scheme is in good agreement with ground measurements. By comparing with existing widely used DSR products based on the same in situ observations, the derived DSR of this study performed better with the smallest RMSE, the lowest absolute value MB and the comparable R values on different spatiotemporal scales. Furthermore, the derived DSR of this study can capture the temporal variation characteristics as revealed by in situ observations. The proposed methodology also provided reasonable spatial distribution patterns. Specifically, this method demonstrated its superiority in characterizing more details and high dynamics of the spatial pattern of DSR due to its higher resolution (1 km) and terrain correction. In addition, the differences in the verification results and spatial distribution of different DSR products also prove that there are still great uncertainties in current DSR products over the TP.

It should be noted that there are still some discrepancies for estimated DSR. Several reasons may contribute to these discrepancies. First, the accuracy of the parameterization method depends on the

accuracy of the input data to some extent, such as cloud and aerosol information. At present, the
545 inhomogeneity of the horizontal and vertical directions of clouds in nature cannot be fully reflected
from the plan-parallel assumption, which is used for most cloud physical parameter inversions (Letu et
al., 2020). The defects will lead to uncertainties in cloud parameters. For the input atmospheric
parameters, the retrieval of AOD is quite challenging. The current popular “dark target” algorithm
cannot deal well with AOD retrievals on bright surfaces, such as snow/ice cover. Some studies have
550 shown that MODIS AOD products have high uncertainties in the TP compared with other regions
(Wang et al., 2007; Xu et al., 2015). Second, there are many snow/ice covers in the TP, while snow/ice
and clouds are hard to distinguish due to their similar reflective optical characteristics in many spectral
regions. The ground radiation field becomes extremely complex when the surface is covered by
snow/ice. These factors make it still a very challenging task to estimate the DSR on snow/ice cover
555 thus far, especially under cloudy-sky conditions. Finally, kilometer-level satellite-based DSR is
susceptible to the 3D radiative effects of clouds. It is difficult to tackle the 3D variability of clouds in
DSR retrieval algorithms, especially for instantaneous DSR (Huang et al., 2019). Furthermore, because
convective clouds are abundant and easily lead to precipitation over the TP (Fu et al., 2020), the 3D
effect of clouds may be more difficult to address on the TP.

560 The improved parameterization scheme can provide an independent reference for surface radiation
budget and land–atmosphere interaction studies over the TP. In this study, topographic effects are
coupled in the DSR parameterization scheme by taking shading and terrain reflections into account.
Sky view factor is also an important factor for DSR in mountainous areas (Ma et al., 2023). Further
improvements may be achieved by introducing the sky view factor into the parameterization scheme.
565 It’s still a great challenge to evaluate DSR products over mountainous areas. Currently, it is difficult to
do fully evaluations for this complex topography due to lack of in situ measurements on different
aspect and slopes over the TP (Yan et al., 2020; Ma et al., 2023). Additionally, the generating of daily
shortwave radiation datasets remains a challenge. New-generation geostationary satellites with higher
temporal and spectral resolutions, such as FengYun-4 and Himawari-8, have been launched
570 successfully (Bessho et al., 2016; Guo et al., 2017). This provides an opportunity to obtain hourly and
daily DSR. Moreover, this allows us to further extend this method to obtain more details of surface
radiation components over the TP in the future.

Appendix A

$$\tau_{b,clr} = \max(0, \tau_a \tau_{oz} \tau_g \tau_w - 0.013) \cos \theta, \quad (A1)$$

$$575 \quad \tau_{d,clr} = \max(0, \tau_{oz} \tau_g \tau_w (1 - \tau_r \tau_a) + 0.013) \frac{(\cos s)^2}{2 \sin \alpha}, \quad (A2)$$

$$\tau_{r,clr} = \rho_g (0.271 + 0.706 \max(0, \tau_a \tau_{oz} \tau_g \tau_w - 0.013)) \frac{(\sin s)^2}{2 \sin \alpha}, \quad (A3)$$

where τ_a , τ_{oz} , τ_g , τ_w and τ_r refer to the broadband radiative transmittance for ozone aerosol extinction (aerosol scattering and absorption), ozone absorption, permanent gas absorption, water vapor absorption, and Rayleigh scattering, respectively. The above transmittances, τ_a , τ_{oz} , τ_g , τ_w , and τ_r ,
580 were obtained primarily by the parameterizations of Yang et al. (2006a).

$$\tau_{b,cld} = \tau_{oz} \tau_w \tau_g \tau_r \tau_a \tau_{cld} \cos \theta, \quad (A4)$$

$$\tau_{d,cld} = (\tau_{d,cld}^{r,ms} + \tau_{d,cld}^{a,ms} + \tau_{d,cld}^{ss,ms}) \frac{(\cos s)^2}{2 \sin \alpha}, \quad (A5)$$

$$\tau_{d,cld}^{r,ms} = 0.5 \tau_{oz} \tau_w \tau_g \tau_{aa} (1 - \tau_r) \tau_{cld,a} \tau_{cld,ms}, \quad (A6)$$

$$\tau_{d,cld}^{a,ms} = f_{aer}(\mu) \tau_{oz} \tau_w \tau_g \tau_{aa} \tau_r (1 - \tau_{as}) \tau_{cld,a} \tau_{cld,ms}, \quad (A7)$$

$$585 \quad \tau_{d,cld}^{ss,ms} = \tau_{oz} \tau_w \tau_g \tau_a \tau_r \tau_{cld,a} (1 - \tau_{cld,ss}) \tau_{cld,ms}, \quad (A8)$$

$$\tau_{r,cld} = \rho_g (0.271 + 0.706 \tau_{oz} \tau_w \tau_g \tau_r \tau_a \tau_{cld}) \frac{(\sin s)^2}{2 \sin \alpha}, \quad (A9)$$

where τ_{cld} , $\tau_{cld,a}$ and $\tau_{cld,ss}$ refer to the broadband radiative transmittance, broadband radiative absorption transmittance and broadband radiative scattering transmittance caused by cloud single-scattering actions, respectively. τ_{aa} , τ_{as} and $\tau_{cld,ms}$ refer to the broadband radiative
590 transmittance for aerosol absorption, aerosol scattering and cloud radiation multiple actions, respectively.

μ is the cosine of the solar zenith angle, and $f_{aer}(\mu)$ is the aerosol forward scattering fraction, which is parameterized as

$$f_{aer}(\mu) = 0.364 + 0.632\mu - 0.245\mu^2, \quad (A10)$$

595 τ_{cld} , $\tau_{cld,a}$, $\tau_{cld,ss}$, $\tau_{cld,ms}$, τ_{aa} , and τ_{as} can be described as follows:

$$\tau_{cld} = \exp(-aCWP/\mu CER), \quad (A11)$$

$$\tau_{cld,a} = \exp(-bCWP/\mu CER), \quad (A12)$$

$$\tau_{cld,ss} = \exp(-c_1\mu CWP^{c_2}/(\mu^{c_2} + c_3CWP^{c_2})), \quad (A13)$$

$$\tau_{cld,ms} = \exp\left(\frac{-CWP/CER}{d_1+d_2CWP/CER+d_3\sqrt{CWP/CER}}\right), \quad (A14)$$

$$600 \quad \tau_{aa} = \tau_a^{(1-\omega_a)}, \quad (A15)$$

$$\tau_{as} = \tau_a^{\omega_a}, \quad (A16)$$

The atmosphere hemispherical albedo $\rho_{a,cld}$ is parameterized as:

$$\rho_{a,cld} = 0.086 + \frac{CWP/CER}{e_1+e_2CWP/CER+e_3\sqrt{CWP/CER}}, \quad (A17)$$

where the coefficients ($a, b, c_1, c_2, c_3, d_1, d_2, d_3, e_1, e_2, e_3$) for different types of clouds can be found in
605 the study by Huang et al. (2018). ω_a is the aerosol single-scattering albedo, and its value depends on the type of aerosol (Levy et al., 2007; Huang et al., 2020).

Here, we assume that ozone absorption and air molecule scattering both take place above clouds (Qin et al., 2015; Tang et al., 2016; Huang et al., 2018). $\tau_{d,cld}^{r,ms}$ and $\tau_{d,cld}^{a,ms}$ can represent the part of diffuse radiation (caused by Rayleigh scattering and aerosol scattering, respectively) that finally
610 reaches the surface after cloud multiscattering. $\tau_{d,cld}^{ss,ms}$ can represent the part of diffuse radiation (caused by cloud single scattering) that finally reaches the surface after cloud multiscattering.

The topographic effects are taken into account in DSR estimation parameterization schemes by the solar zenith angle θ , the solar altitude angle α and the tilt angle of the surface (slope) s . According to this knowledge, Chen et al. (2013) provided a scheme that can be applied in mountainous
615 areas based on high-resolution DEM datasets.

$$\sin \alpha = \sin L \sin \delta_s + \cos L \cos \delta_s \cos h_s, \quad (A18)$$

$$\cos \theta = \sin L \sin \delta_s \cos s - \cos L \sin \delta_s \sin s \cos \gamma$$

$$+ \cos L \cos \delta_s \cos s \cos h_s + \sin L \cos \delta_s \sin s \cos \gamma \cos h_s$$

$$+ \sin L \cos \delta_s \sin s \sin h_s, \quad (A19)$$

620 where L is latitude. δ_s is the declination of the earth. h_s is the hour angle. γ is the surface aspect angle.

The BSA and WSA are the surface albedos under the condition of complete direct and diffuse

solar radiation, not the actual surface albedo. According to Pinty et al. (2005) and Stokes and Schwartz (1994), the actual surface albedo can be obtained by

$$625 \quad r = 0.122 + 0.85 \exp(-4.8\mu), \quad (\text{A20})$$

$$\rho_g = rBSA + (1 - r)WSA, \quad (\text{A21})$$

The precipitable water w (cm) is estimated from relative humidity RH (%) and air temperature T_{air} (K) by a semiempirical formula (Yang et al., 2006; Yang et al., 2010):

$$w = 0.00493RH T_{\text{air}}^{-1} \exp(26.23 - 5416T_{\text{air}}^{-1}), \quad (\text{A22})$$

630 **Data availability**

The in situ measurements used in this study were obtained from the National Tibetan Plateau Data Center (<http://data.tpdc.ac.cn>) and National Cryosphere Desert Data Center (<http://www.ncdc.ac.cn>). The MODIS products we used can be freely downloaded via the NASA website (<https://modis.gsfc.nasa.gov/>).

635 **Author contributions.**

PL and ZL designed and implemented the study. PL prepared the manuscript with help from ZL, YM and YF. MC and XW contributed to analysis of the data. YQ and ZW collected the in situ data. All commented on the paper.

Acknowledgments

640 This work was funded by the Second Tibetan Plateau Scientific Expedition and Research (STEP) Program (Grant No. 2019QZKK0103); The Chinese Academy of Sciences (Grant No. XDA20060101); National Natural Science Foundation of China (Grant No. 41875031, 91837208, 41522501, 41275028) and CLIMATE-Pan-TPE in the framework of the ESA-MOST Dragon 5 Programme (Grant ID 58516).

Competing interests.

645 The authors declare that they have no conflict of interest.

Reference

- Ahn, C., Torres, O., and Bhartia, P. K.: Comparison of ozone monitoring instrument UV aerosol products with Aqua/Moderate Resolution Imaging Spectroradiometer and multiangle imaging spectroradiometer observations in 2006, *Journal of Geophysical Research*, 113, 650 10.1029/2007jd008832, 2008.
- Bessho, K., Date, K., Hayashi, M., Ikeda, A., Imai, T., Inoue, H., Kumagai, Y., Miyakawa, T., Murata, H., Ohno, T., Okuyama, A., Oyama, R., Sasaki, Y., Shimazu, Y., Shimoji, K., Sumida, Y., Suzuki, M., Taniguchi, H., Tsuchiyama, H., Uesawa, D., Yokota, H., and Yoshida, R.: An introduction to Himawari-8/9—Japan's new-generation geostationary meteorological satellites, *Journal of the Meteorological Society of Japan*. Ser. II, 94, 151-183, 10.2151/jmsj.2016-009, 2016. 655
- Bisht, G. and Bras, R. L.: Estimation of net radiation from the MODIS data under all sky conditions: Southern Great Plains case study, *Remote Sensing of Environment*, 114, 1522-1534, 10.1016/j.rse.2010.02.007, 2010.
- Bisht, G., Venturini, V., Islam, S., and Jiang, L.: Estimation of the net radiation using MODIS (Moderate Resolution Imaging Spectroradiometer) data for clear sky days, *Remote Sensing of Environment*, 97, 52-67, 10.1016/j.rse.2005.03.014, 2005. 660
- Chen, J., Hu, Z., Dou, S., and Zeyu, Q.: Yin–Yang Slope problem along Qinghai–Tibetan Lines and its radiation mechanism, *Cold Regions Science and Technology*, 44, 217-224, 10.1016/j.coldregions.2005.12.001, 2006.
- 665 Chen, X., Su, Z., Ma, Y., Yang, K., and Wang, B.: Estimation of surface energy fluxes under complex terrain of Mt. Qomolangma over the Tibetan Plateau, *Hydrology and Earth System Sciences*, 17, 1607-1618, 10.5194/hess-17-1607-2013, 2013.
- Decker, M., Brunke, M. A., Wang, Z., Sakaguchi, K., Zeng, X., and Bosilovich, M. G.: Evaluation of the reanalysis products from GSFC, NCEP, and ECMWF using flux tower observations, *Journal of Climate*, 25, 1916-1944, 10.1175/jcli-d-11-00004.1, 2012. 670
- Fu, Y., Ma, Y., Zhong, L., Yang, Y., Guo, X., Wang, C., Xu, X., Yang, K., Xu, X., Liu, L., Fan, G., Li, Y., and Wang, D.: Land-surface processes and summer-cloud-precipitation characteristics in the Tibetan Plateau and their effects on downstream weather: a review and perspective, *Natl Sci Rev*, 7, 500-515, 10.1093/nsr/nwz226, 2020.

- 675 Fujinami, H., Nomura, S., and Yasunari, T.: Characteristics of diurnal variations in convection and precipitation over the southern Tibetan Plateau during summer, *Sola*, 1, 49-52, 10.2151/sola.2005-014, 2005.
- Gueymard, C. A.: Clear-sky irradiance predictions for solar resource mapping and large-scale applications: Improved validation methodology and detailed performance analysis of 18
680 broadband radiative models, *Solar Energy*, 86, 2145-2169, 10.1016/j.solener.2011.11.011, 2012.
- Guo, Q., Lu, F., Wei, C., Zhang, Z., and Yang, J.: Introducing the new generation of Chinese geostationary weather satellites, Fengyun-4, *Bulletin of the American Meteorological Society*, 98, 1637-1658, 10.1175/bams-d-16-0065.1, 2017.
- Hakuba, M. Z., Folini, D., Sanchez-Lorenzo, A., and Wild, M.: Spatial representativeness of
685 ground-based solar radiation measurements, *Journal of Geophysical Research: Atmospheres*, 118, 8585-8597, 10.1002/jgrd.50673, 2013.
- Hans, H., Bell, W., Berrisford, P., Andras, H., Muñoz-Sabater, J., Nicolas, J., Raluca, R., Dinand, S., Adrian, S., Cornel, S., and Dick, D.: Global reanalysis: goodbye ERA-Interim, hello ERA5, 2019.
- 690 He, J., Yang, K., Tang, W., Lu, H., Qin, J., Chen, Y., and Li, X.: The first high-resolution meteorological forcing dataset for land process studies over China, *Sci Data*, 7, 25, 10.1038/s41597-020-0369-y, 2020.
- Hong, S.-Y., Kanamitsu, M., Kim, J.-E., and Koo, M.-S.: Effects of diurnal cycle on a simulated Asian summer monsoon, *Journal of Climate*, 25, 8394-8408, 10.1175/jcli-d-12-00069.1, 2012.
- 695 Huang, C., Shi, H., Gao, L., Liu, M., Chen, Q., Fu, D., Wang, S., Yuan, Y., and Xia, X. a.: Fengyun-4 geostationary satellite-based solar energy nowcasting system and its application in North China, *Adv Atmos Sci*, 39, 1316-1328, 10.1007/s00376-022-1464-0, 2022.
- Huang, G., Li, X., Lu, N., Wang, X., and He, T.: A general parameterization scheme for the estimation of incident photosynthetically active radiation under cloudy skies, *IEEE Transactions on
700 Geoscience and Remote Sensing*, 58, 6255-6265, 10.1109/tgrs.2020.2976103, 2020.
- Huang, G., Li, X., Ma, M., Li, H., and Huang, C.: High resolution surface radiation products for studies of regional energy, hydrologic and ecological processes over Heihe river basin, northwest China, *Agric. For. Meteorol*, 230-231, 67-78, 10.1016/j.agrformet.2016.04.007, 2016a.

- Huang, G., Liang, S., Lu, N., Ma, M., and Wang, D.: Toward a broadband parameterization scheme for
705 estimating surface solar irradiance: Development and preliminary results on MODIS products,
Journal of Geophysical Research: Atmospheres, 123, 1180-1193, 10.1029/2018jd028905,
2018.
- Huang, G., Li, X., Huang, C., Liu, S., Ma, Y., and Chen, H.: Representativeness errors of point-scale
ground-based solar radiation measurements in the validation of remote sensing products, Remote
710 Sensing of Environment, 181, 198-206, 10.1016/j.rse.2016.04.001, 2016b.
- Huang, G., Li, Z., Li, X., Liang, S., Yang, K., Wang, D., and Zhang, Y.: Estimating surface solar
irradiance from satellites: Past, present, and future perspectives, Remote Sensing of Environment,
233, 10.1016/j.rse.2019.111371, 2019.
- Hwang, K., Choi, M., Lee, S. O., and Seo, J.-W.: Estimation of instantaneous and daily net radiation
715 from MODIS data under clear sky conditions: a case study in East Asia, Irrigation Science, 31,
1173-1184, 10.1007/s00271-012-0396-3, 2012.
- Immerzeel, W. W., van Beek, L. P., and Bierkens, M. F.: Climate change will affect the Asian water
towers, Science, 328, 1382-1385, 10.1126/science.1183188, 2010.
- Kim, D.-H.: Aerosol optical properties over east Asia determined from ground-based sky radiation
720 measurements, Journal of Geophysical Research, 109, 10.1029/2003jd003387, 2004.
- Kuang, X. and Jiao, J. J.: Review on climate change on the Tibetan Plateau during the last half century,
Journal of Geophysical Research: Atmospheres, 121, 3979-4007, 10.1002/2015jd024728, 2016.
- Kukulies, J., Chen, D., and Wang, M.: Temporal and spatial variations of convection, clouds and
precipitation over the Tibetan Plateau from recent satellite observations. Part II: Precipitation
725 climatology derived from global precipitation measurement mission, International Journal of
Climatology, 40, 4858-4875, 10.1002/joc.6493, 2020.
- Letu, H., Nakajima, T. Y., Wang, T., Shang, H., Ma, R., Yang, K., Baran, A. J., Riedi, J., Ishimoto, H.,
Yoshida, M., Shi, C., Khatri, P., Du, Y., Chen, L., and Shi, J.: A new benchmark for surface
radiation products over the East Asia–Pacific region retrieved from the Himawari-8/AHI
730 next-generation geostationary satellite, Bulletin of the American Meteorological Society, 103,
E873-E888, 10.1175/bams-d-20-0148.1, 2022.
- Letu, H., Shi, J., Li, M., Wang, T., Shang, H., Lei, Y., Ji, D., Wen, J., Yang, K., and Chen, L.: A review

- of the estimation of downward surface shortwave radiation based on satellite data: Methods, progress and problems, *Science China Earth Sciences*, 63, 774-789, 10.1007/s11430-019-9589-0, 735 2020.
- Levy, R. C., Remer, L. A., and Dubovik, O.: Global aerosol optical properties and application to Moderate Resolution Imaging Spectroradiometer aerosol retrieval over land, *Journal of Geophysical Research: Atmospheres*, 112, 10.1029/2006jd007815, 2007.
- Li, J., Tang, W., Yang, K., Xie, Y., Gueymard, C. A., Qin, J., and Sengupta, M.: An improved algorithm 740 for estimating surface shortwave radiation: Preliminary evaluation with MODIS products, *IEEE Transactions on Geoscience and Remote Sensing*, 60, 1-9, 10.1109/tgrs.2021.3098742, 2022.
- Li, Y., Wang, Y., Song, Y., Hu, L., Gao, S., and Rong, F.: Characteristics of summer convective systems initiated over the Tibetan Plateau. Part I: Origin, track, development, and precipitation, *Journal of Applied Meteorology and Climatology*, 47, 2679-2695, 10.1175/2008jamc1695.1, 2008.
- 745 Li, Z., Lyu, S., Wen, L., Zhao, L., Ao, Y., and Meng, X.: Study of freeze-thaw cycle and key radiation transfer parameters in a Tibetan Plateau lake using LAKE2.0 model and field observations, *Journal of Glaciology*, 67, 91-106, 10.1017/jog.2020.87, 2020.
- Li, Z., Lyu, S., Wen, L., Zhao, L., Ao, Y., and Wang, S.: Effect of a cold, dry air incursion on atmospheric boundary layer processes over a high-altitude lake in the Tibetan Plateau, 750 *Atmospheric Research*, 185, 32-43, 10.1016/j.atmosres.2016.10.024, 2017.
- Li, Z., Lyu, S., Chen, S., Ao, Y., Zhao, L., Chen, H., and Meng, X.: Observed characteristics of the water and heat transfer of the soil–snow–atmosphere system through the snowpack in the eastern Tibetan Plateau, *Atmospheric Research*, 248, 10.1016/j.atmosres.2020.105195, 2021.
- Li, Z. Q., Barker, H. W., and Moreau, L.: The variable effect of clouds on atmospheric absorption of 755 solar-radiation, *Nature*, 376, 486-490, DOI 10.1038/376486a0, 1995.
- Li, Z. Q., Moreau, L., and Arking, A.: On solar energy disposition: A perspective from observation and modeling, *Bulletin of the American Meteorological Society*, 78, 53-70, Doi 10.1175/1520-0477(1997)078<0053:Osedap>2.0.Co;2, 1997.
- Liang, S., Wang, D., He, T., and Yu, Y.: Remote sensing of earth's energy budget: synthesis and review, 760 *International Journal of Digital Earth*, 12, 737-780, 10.1080/17538947.2019.1597189, 2019.
- Liang, S., Wang, K., Zhang, X., and Wild, M.: Review on estimation of land surface radiation and

- energy budgets from ground measurement, remote sensing and model simulations, *IEEE Journal of Selected Topics in Applied Earth Observations and Remote Sensing*, 3, 225-240, 10.1109/jstars.2010.2048556, 2010.
- 765 Liang, S., Zheng, T., Liu, R., Fang, H., Tsay, S.-C., and Running, S.: Estimation of incident photosynthetically active radiation from Moderate Resolution Imaging Spectrometer data, *Journal of Geophysical Research*, 111, 10.1029/2005jd006730, 2006.
- Loeb, N. G., Kato, S., Rose, F. G., Doelling, D. R., Rutan, D. A., Caldwell, T. E., Yu, L., and Weller, R. A.: Surface irradiances consistent with CERES-derived top-of-atmosphere shortwave and
770 longwave irradiances, *Journal of Climate*, 26, 2719-2740, 10.1175/jcli-d-12-00436.1, 2013.
- Lu, N., Liu, R., Liu, J., and Liang, S.: An algorithm for estimating downward shortwave radiation from GMS 5 visible imagery and its evaluation over China, *Journal of Geophysical Research*, 115, 10.1029/2009jd013457, 2010.
- Lu, N., Qin, J., Yang, K., and Sun, J.: A simple and efficient algorithm to estimate daily global solar
775 radiation from geostationary satellite data, *Energy*, 36, 3179-3188, 10.1016/j.energy.2011.03.007, 2011.
- Ma, R., Letu, H., Yang, K., Wang, T., Shi, C., Xu, J., Shi, J., Shi, C., and Chen, L.: Estimation of surface shortwave radiation from Himawari-8 satellite data based on a combination of radiative transfer and deep neural network, *IEEE Transactions on Geoscience and Remote Sensing*, 58,
780 5304-5316, 10.1109/tgrs.2019.2963262, 2020a.
- Ma, Y., Ma, W., Zhong, L., Hu, Z., Li, M., Zhu, Z., Han, C., Wang, B., and Liu, X.: Monitoring and modeling the Tibetan Plateau's climate system and its impact on East Asia, *Sci Rep*, 7, 44574, 10.1038/srep44574, 2017.
- Ma, Y., Zhu, Z., Zhong, L., Wang, B., Han, C., Wang, Z., Wang, Y., Lu, L., Amatya, P. M., Ma, W., and
785 Hu, Z.: Combining MODIS, AVHRR and in situ data for evapotranspiration estimation over heterogeneous landscape of the Tibetan Plateau, *Atmospheric Chemistry and Physics*, 14, 1507-1515, 10.5194/acp-14-1507-2014, 2014.
- Ma, Y., Wang, Y., Wu, R., Hu, Z., Yang, K., Li, M., Ma, W., Zhong, L., Sun, F., Chen, X., Zhu, Z., Wang, S., and Ishikawa, H.: Recent advances on the study of atmosphere-land interaction
790 observations on the Tibetan Plateau, *Hydrology and Earth System Sciences*, 13, 1103-1111, DOI

10.5194/hess-13-1103-2009, 2009.

Ma, Y., Hu, Z., Xie, Z., Ma, W., Wang, B., Chen, X., Li, M., Zhong, L., Sun, F., Gu, L., Han, C., Zhang, L., Liu, X., Ding, Z., Sun, G., Wang, S., Wang, Y., and Wang, Z.: A long-term (2005–2016) dataset of hourly integrated land–atmosphere interaction observations on the Tibetan Plateau, Earth
795 System Science Data, 12, 2937-2957, 10.5194/essd-12-2937-2020, 2020b.

Ma, Y. M., Kang, S. C., Zhu, L. P., Xu, B. Q., Tian, L. D., and Yao, T. D.: Tibetan observation and research platform atmosphere-land interaction over a heterogeneous landscape, Bulletin of the American Meteorological Society, 89, 1487-+, 10.1175/2008bams2545.1, 2008.

Masuda, K., Leighton, H. G., and Li, Z. Q.: A new parameterization for the determination of solar flux absorbed at the surface from satellite measurements, Journal of Climate, 8, 1615-1629, Doi
800 10.1175/1520-0442(1995)008<1615:Anpftd>2.0.Co;2, 1995.

Ma, Y., He, T., Liang, S., McVicar, T. R., Hao, D., Liu, T., and Jiang, B.: Estimation of fine spatial resolution all-sky surface net shortwave radiation over mountainous terrain from Landsat 8 and Sentinel-2 data, Remote Sensing of Environment, 285, 10.1016/j.rse.2022.113364, 2023.

805 Niemela, S., Raisanen, P., and Savijarvi, H.: Comparison of surface radiative flux parameterizations - Part II. Shortwave radiation, Atmospheric Research, 58, 141-154, 10.1016/S0169-8095(01)00085-0, 2001.

Olson, M. and Rupper, S.: Impacts of topographic shading on direct solar radiation for valley glaciers in complex topography, The Cryosphere, 13, 29-40, 10.5194/tc-13-29-2019, 2019.

810 Piao, S., Ciais, P., Huang, Y., Shen, Z., Peng, S., Li, J., Zhou, L., Liu, H., Ma, Y., Ding, Y., Friedlingstein, P., Liu, C., Tan, K., Yu, Y., Zhang, T., and Fang, J.: The impacts of climate change on water resources and agriculture in China, Nature, 467, 43-51, 10.1038/nature09364, 2010.

Pinker, R. T. and Laszlo, I.: Modeling surface solar irradiance for satellite applications on a global scale, J Appl Meteorol, 31, 194-211, Doi 10.1175/1520-0450(1992)031<0194:Mssifs>2.0.Co;2, 1992.

815 Pinker, R. T., Zhang, B., and Dutton, E. G.: Do satellites detect trends in surface solar radiation?, Science, 308, 850-854, 10.1126/science.1103159, 2005.

Pinker, R. T., Li, X., Meng, W., and Yegorova, E. A.: Toward improved satellite estimates of short-wave radiative fluxes—Focus on cloud detection over snow: 2. Results, Journal of Geophysical Research, 112, 10.1029/2005jd006699, 2007.

- 820 Pinty, B., Lattanzio, A., Martonchik, J. V., Verstraete, M. M., Gobron, N., Taberner, M., Widlowski, J. L., Dickinson, R. E., and Govaerts, Y.: Coupling diffuse sky radiation and surface albedo, *Journal of the Atmospheric Sciences*, 62, 2580-2591, Doi 10.1175/Jas3479.1, 2005.
- Platnick, S., King, M. D., Ackerman, S. A., Menzel, W. P., Baum, B. A., Riedi, J. C., and Frey, R. A.: The MODIS cloud products: algorithms and examples from terra, *IEEE Transactions on Geoscience and Remote Sensing*, 41, 459-473, 10.1109/tgrs.2002.808301, 2003.
- 825 Platnick, S., Meyer, K. G., King, M. D., Wind, G., Amarasinghe, N., Marchant, B., Arnold, G. T., Zhang, Z., Hubanks, P. A., Holz, R. E., Yang, P., Ridgway, W. L., and Riedi, J.: The MODIS cloud optical and microphysical products: Collection 6 updates and examples from Terra and Aqua, *IEEE Trans Geosci Remote Sens*, 55, 502-525, 10.1109/TGRS.2016.2610522, 2017.
- 830 Qin, J., Chen, Z., Yang, K., Liang, S., and Tang, W.: Estimation of monthly-mean daily global solar radiation based on MODIS and TRMM products, *Applied Energy*, 88, 2480-2489, 10.1016/j.apenergy.2011.01.018, 2011.
- Qin, J., Tang, W., Yang, K., Lu, N., Niu, X., and Liang, S.: An efficient physically based parameterization to derive surface solar irradiance based on satellite atmospheric products, *Journal of Geophysical Research: Atmospheres*, 120, 4975-4988, 10.1002/2015jd023097, 2015.
- 835 Qiu, J.: The third pole, *NATURE*, 454, 393-396, 10.1038/454393a, 2008.
- Roupioz, L., Jia, L., Nerry, F., and Menenti, M.: Estimation of daily solar radiation budget at kilometer resolution over the Tibetan Plateau by integrating MODIS data products and a DEM, *Remote Sensing*, 8, 10.3390/rs8060504, 2016.
- 840 Schaaf, C. B., Gao, F., Strahler, A. H., Lucht, W., Li, X. W., Tsang, T., Strugnell, N. C., Zhang, X. Y., Jin, Y. F., Muller, J. P., Lewis, P., Barnsley, M., Hobson, P., Disney, M., Roberts, G., Dunderdale, M., Doll, C., d'Entremont, R. P., Hu, B. X., Liang, S. L., Privette, J. L., and Roy, D.: First operational BRDF, albedo nadir reflectance products from MODIS, *Remote Sensing of Environment*, 83, 135-148, 10.1016/S0034-4257(02)00091-3, 2002.
- 845 Sengupta, M., Xie, Y., Lopez, A., Habte, A., Maclaurin, G., and Shelby, J.: The National Solar Radiation Data Base (NSRDB), *Renewable and Sustainable Energy Reviews*, 89, 51-60, 10.1016/j.rser.2018.03.003, 2018.
- Stephens, G. L., Li, J., Wild, M., Clayson, C. A., Loeb, N., Kato, S., L'Ecuyer, T., Stackhouse, P. W.,

- Lebsock, M., and Andrews, T.: An update on Earth's energy balance in light of the latest global
850 observations, *Nature Geoscience*, 5, 691-696, 10.1038/ngeo1580, 2012.
- Stokes, G. M. and Schwartz, S. E.: The Atmospheric Radiation - Measurement (Arm) program -
programmatic background and design of the cloud and radiation Test-Bed, *Bulletin of the
American Meteorological Society*, 75, 1201-1221, Doi
10.1175/1520-0477(1994)075<1201:Tarmpp>2.0.Co;2, 1994.
- 855 Tanaka, K., Ishikawa, H., Hayashi, T., Tamagawa, I., and Ma, Y. M.: Surface energy budget at Amdo on
the Tibetan Plateau using GAME/Tibet IOP98 data, *J Meteorol Soc Jpn*, 79, 505-517, DOI
10.2151/jmsj.79.505, 2001.
- Tang, W., Yang, K., Qin, J., Li, X., and Niu, X.: A 16-year dataset (2000–2015) of high-resolution (3 h,
10 km) global surface solar radiation, *Earth System Science Data*, 11, 1905-1915,
860 10.5194/essd-11-1905-2019, 2019.
- Tang, W., Qin, J., Yang, K., Liu, S., Lu, N., and Niu, X.: Retrieving high-resolution surface solar
radiation with cloud parameters derived by combining MODIS and MTSAT data, *Atmospheric
Chemistry and Physics*, 16, 2543-2557, 10.5194/acp-16-2543-2016, 2016.
- Tovar, J., Olmo, F. J., and Aladosarboledas, L.: Local-scale variability of solar-radiation in a
865 mountainous region, *J Appl Meteorol*, 34, 2316-2322,
10.1175/1520-0450(1995)034<2316:LSVOSR>2.0.CO;2, 1995.
- Wang, D., Liang, S., Zhang, Y., Gao, X., Brown, M. G. L., and Jia, A.: A new set of MODIS land
products (MCD18): Downward shortwave radiation and photosynthetically active radiation,
Remote Sensing, 12, 10.3390/rs12010168, 2020.
- 870 Wang, G., Wang, T., and Xue, H.: Validation and comparison of surface shortwave and longwave
radiation products over the three poles, *International Journal of Applied Earth Observation and
Geoinformation*, 104, 10.1016/j.jag.2021.102538, 2021.
- Wang, K. and Dickinson, R. E.: Contribution of solar radiation to decadal temperature variability over
land, *Proc Natl Acad Sci U S A*, 110, 14877-14882, 10.1073/pnas.1311433110, 2013.
- 875 Wang, L., Gong, W., Hu, B., Lin, A., Li, H., and Zou, L.: Modeling and analysis of the spatiotemporal
variations of photosynthetically active radiation in China during 1961–2012, *Renewable and
Sustainable Energy Reviews*, 49, 1019-1032, 10.1016/j.rser.2015.04.174, 2015.

- Wang, L., Xin, J., Wang, Y., Li, Z., Liu, G., and Li, J.: Evaluation of the MODIS aerosol optical depth retrieval over different ecosystems in China during EAST-AIRE, *Atmospheric Environment*, 41, 880 7138-7149, 10.1016/j.atmosenv.2007.05.001, 2007.
- Wei, Y., Zhang, X., Hou, N., Zhang, W., Jia, K., and Yao, Y.: Estimation of surface downward shortwave radiation over China from AVHRR data based on four machine learning methods, *Solar Energy*, 177, 32-46, 10.1016/j.solener.2018.11.008, 2019.
- Wu, G., Liu, Y., He, B., Bao, Q., Duan, A., and Jin, F. F.: Thermal controls on the Asian summer 885 monsoon, *Sci Rep*, 2, 404, 10.1038/srep00404, 2012.
- Xie, Y., Sengupta, M., and Dudhia, J.: A Fast All-sky Radiation Model for Solar applications (FARMS): Algorithm and performance evaluation, *Solar Energy*, 135, 435-445, 10.1016/j.solener.2016.06.003, 2016.
- Xu, C., Ma, Y. M., You, C., and Zhu, Z. K.: The regional distribution characteristics of aerosol optical 890 depth over the Tibetan Plateau, *Atmospheric Chemistry and Physics*, 15, 12065-12078, 10.5194/acp-15-12065-2015, 2015.
- Xu, W., Ma, L., Ma, M., Zhang, H., and Yuan, W.: Spatial-temporal variability of snow cover and depth in the Qinghai-Tibetan Plateau, *Journal of Climate*, 30, 1521-1533, 10.1175/jcli-d-15-0732.1, 2017.
- 895 Xu, X., Lu, C., Shi, X., and Gao, S.: World water tower: An atmospheric perspective, *Geophysical Research Letters*, 35, 10.1029/2008gl035867, 2008.
- Yang, D., Wang, W., and Xia, X. a.: A concise overview on solar resource assessment and forecasting, *Adv Atmos Sci*, 39, 1239-1251, 10.1007/s00376-021-1372-8, 2022.
- Yang, K., Koike, T., and Ye, B.: Improving estimation of hourly, daily, and monthly solar radiation by 900 importing global data sets, *Agric. For. Meteorol*, 137, 43-55, 10.1016/j.agrformet.2006.02.001, 2006a.
- Yang, K., He, J., Tang, W., Qin, J., and Cheng, C. C. K.: On downward shortwave and longwave radiations over high altitude regions: Observation and modeling in the Tibetan Plateau, *Agric. For. Meteorol*, 150, 38-46, 10.1016/j.agrformet.2009.08.004, 2010a.
- 905 Yang, K., Koike, T., Stackhouse, P., Mikovitz, C., and Cox, S. J.: An assessment of satellite surface radiation products for highlands with Tibet instrumental data, *Geophysical Research Letters*, 33,

10.1029/2006gl027640, 2006b.

910 Yang, K., Wu, H., Qin, J., Lin, C., Tang, W., and Chen, Y.: Recent climate changes over the Tibetan Plateau and their impacts on energy and water cycle: A review, *Global and Planetary Change*, 112, 79-91, 10.1016/j.gloplacha.2013.12.001, 2014.

Yang, K., Pinker, R. T., Ma, Y., Koike, T., Wonsick, M. M., Cox, S. J., Zhang, Y., and Stackhouse, P.: Evaluation of satellite estimates of downward shortwave radiation over the Tibetan Plateau, *Journal of Geophysical Research*, 113, 10.1029/2007jd009736, 2008.

915 Yang, M., Nelson, F. E., Shiklomanov, N. I., Guo, D., and Wan, G.: Permafrost degradation and its environmental effects on the Tibetan Plateau: A review of recent research, *Earth-Science Reviews*, 103, 31-44, 10.1016/j.earscirev.2010.07.002, 2010b.

Yan, G., Chu, Q., Tong, Y., Mu, X., Qi, J., Zhou, Y., Liu, Y., Wang, T., Xie, D., Zhang, W., Yan, K., Chen, S., and Zhou, H.: An operational method for validating the downward shortwave radiation over rugged terrains, *IEEE Transactions on Geoscience and Remote Sensing*, 1-18, 920 10.1109/tgrs.2020.2994384, 2020.

Yao, J., Zhao, L., Gu, L., Qiao, Y., and Jiao, K.: The surface energy budget in the permafrost region of the Tibetan Plateau, *Atmospheric Research*, 102, 394-407, 10.1016/j.atmosres.2011.09.001, 2011.

Yao, T., Thompson, L., Yang, W., Yu, W., Gao, Y., Guo, X., Yang, X., Duan, K., Zhao, H., Xu, B., Pu, J., Lu, A., Xiang, Y., Kattel, D. B., and Joswiak, D.: Different glacier status with atmospheric 925 circulations in Tibetan Plateau and surroundings, *Nature Climate Change*, 2, 663-667, 10.1038/nclimate1580, 2012.

Zhang, H., Xin, X., Li, L., and Liu, Q.: Estimating global solar radiation using a hybrid parametric model from MODIS data over the Tibetan Plateau, *Solar Energy*, 112, 373-382, 10.1016/j.solener.2014.12.015, 2015.

930 Zhang, J., Zhao, L., Deng, S., Xu, W., and Zhang, Y.: A critical review of the models used to estimate solar radiation, *Renewable and Sustainable Energy Reviews*, 70, 314-329, 10.1016/j.rser.2016.11.124, 2017.

Zhang, K., Zhao, L., Tang, W., Yang, K., and Wang, J.: Global and regional evaluation of the CERES 935 edition-4A surface solar radiation and its uncertainty quantification, *IEEE Journal of Selected Topics in Applied Earth Observations and Remote Sensing*, 15, 2971-2985,

10.1109/jstars.2022.3164471, 2022.

Zhang, T., Stackhouse, P. W., Chandler, W. S., and Westberg, D. J.: Application of a global-to-beam irradiance model to the NASA GEWEX SRB dataset: An extension of the NASA surface meteorology and solar energy datasets, *Solar Energy*, 110, 117-131, 10.1016/j.solener.2014.09.006, 940 2014.

Zhao, C., Chen, Y., Li, J., Letu, H., Su, Y., Chen, T., and Wu, X.: Fifteen-year statistical analysis of cloud characteristics over China using Terra and Aqua Moderate Resolution Imaging Spectroradiometer observations, *International Journal of Climatology*, 39, 2612-2629, 10.1002/joc.5975, 2019a.

945 Zhao, L., Zou, D., Hu, G., Wu, T., Du, E., Liu, G., Xiao, Y., Li, R., Pang, Q., Qiao, Y., Wu, X., Sun, Z., Xing, Z., Sheng, Y., Zhao, Y., Shi, J., Xie, C., Wang, L., Wang, C., and Cheng, G.: A synthesis dataset of permafrost thermal state for the Qinghai–Tibet (Xizang) Plateau, China, *Earth System Science Data*, 13, 4207-4218, 10.5194/essd-13-4207-2021, 2021.

Zhao, P., Zhou, X., Chen, J., Liu, G., and Nan, S.: Global climate effects of summer Tibetan Plateau, 950 *Science Bulletin*, 64, 1-3, 10.1016/j.scib.2018.11.019, 2019b.

Zhao, P., Xu, X., Chen, F., Guo, X., Zheng, X., Liu, L., Hong, Y., Li, Y., La, Z., Peng, H., Zhong, L., Ma, Y., Tang, S., Liu, Y., Liu, H., Li, Y., Zhang, Q., Hu, Z., Sun, J., Zhang, S., Dong, L., Zhang, H., Zhao, Y., Yan, X., Xiao, A., Wan, W., Liu, Y., Chen, J., Liu, G., Zhaxi, Y., and Zhou, X.: The third atmospheric scientific experiment for understanding the earth–atmosphere coupled system over 955 the Tibetan Plateau and its effects, *Bulletin of the American Meteorological Society*, 99, 757-776, 10.1175/bams-d-16-0050.1, 2018.

Zhong, L., Ma, Y., Su, Z., and Salama, M. S.: Estimation of land surface temperature over the Tibetan Plateau using AVHRR and MODIS data, *Adv Atmos Sci*, 27, 1110-1118, 10.1007/s00376-009-9133-0, 2010.

960 Zhong, L., Ma, Y., Hu, Z., Fu, Y., Hu, Y., Wang, X., Cheng, M., and Ge, N.: Estimation of hourly land surface heat fluxes over the Tibetan Plateau by the combined use of geostationary and polar-orbiting satellites, *Atmospheric Chemistry and Physics*, 19, 5529-5541, 10.5194/acp-19-5529-2019, 2019a.

Zhong, L., Zou, M., Ma, Y., Huang, Z., Xu, K., Wang, X., Ge, N., and Cheng, M.: Estimation of

965 downwelling shortwave and longwave radiation in the Tibetan Plateau under all-sky conditions,
Journal of Geophysical Research: Atmospheres, 124, 11086-11102, 10.1029/2019jd030763,
2019b.

Zhou, Y., Li, Z., Li, J., Zhao, R., and Ding, X.: Glacier mass balance in the Qinghai–Tibet Plateau and
its surroundings from the mid-1970s to 2000 based on Hexagon KH-9 and SRTM DEMs, Remote
970 Sensing of Environment, 210, 96-112, 10.1016/j.rse.2018.03.020, 2018.